Part II

Lumped Parameter Model

5
Multi-compressor multi-evaporator direct expansion refrigeration system

Hereafter, the lumped parameter model for the steady-state operation of a typical supermarket direct expansion (DX) system is developed and simulated.

5.1
Overview

The present model simulates a DX refrigeration system operating at steady-state condition, taking into account the pressure drop and heat transfer phenomena in all the components. Superheat at compressor inlet and subcooling at condenser outlet are prescribed variables. Another characteristic of the model developed is the ability to deal with multiple in-parallel evaporators and compressors, as is usually the case of a typical commercial refrigeration system. The component-based simulation model is composed of sub-models, one for each component: compressor (cp), discharge line (dl), condenser (cd), liquid line (ll), expansion device (xd), evaporator (ev) and suction line (sl). To describe each of them, energy, momentum and mass balance equations are applied, together with heat transfer laws.

Figure 5.1, which is an adaptation of a supermarket system schematics from Rinne et al. [136], illustrates the multi-compressor multi-evaporator DX system modeled. A more detailed description of the processes taking place in each component can be found in Section 4.1.

The most relevant characteristic of the model resides in the detailed multi-zone analysis of the heat exchangers. Each of the evaporators is divided in two portions: two-phase and superheated, whilst the condenser accounts for three regions: superheated, two-phase and subcooled. Previous experience of the industry proved that this is a reasonable approach for performance trend analysis, which is essentially the main objective of this study, though limited when design and optimization are envisioned.

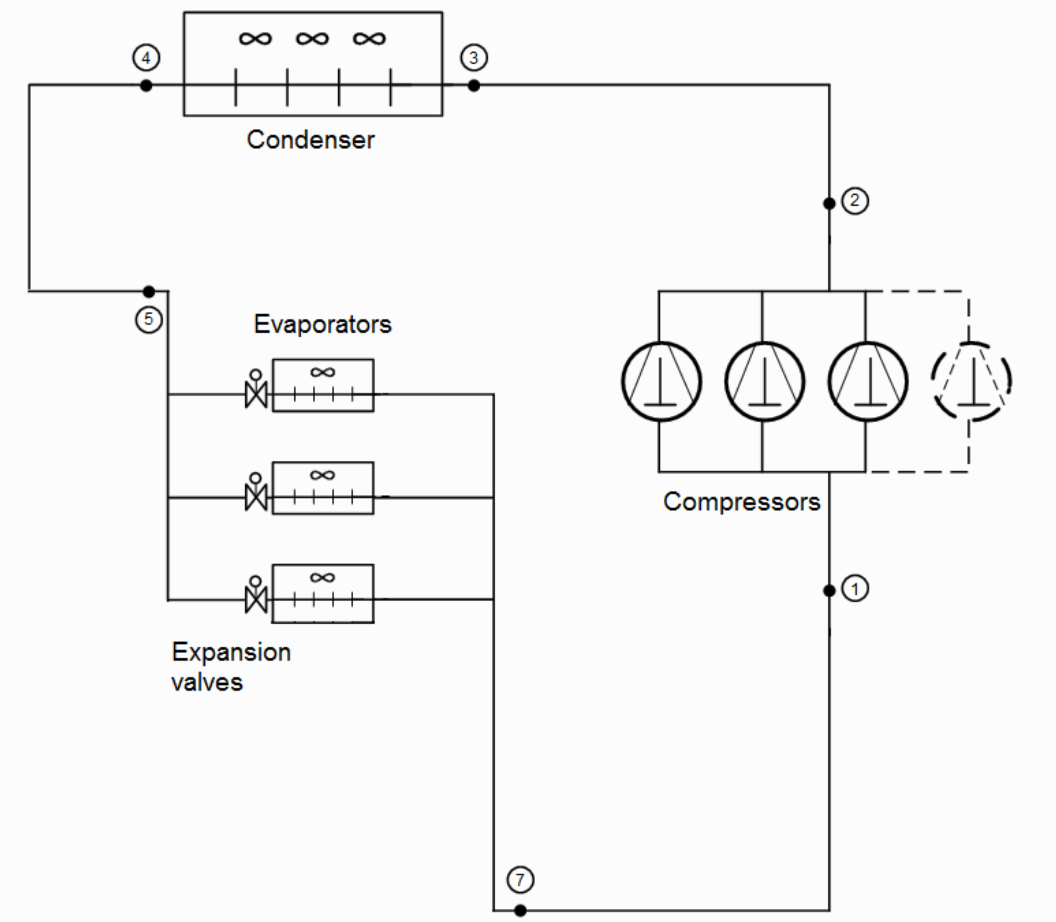

Figure 5.1: Simplified version of a supermarket direct expansion system, adapted from Rinne et al. [136].

5.2 Mathematical model

As a first hyphotesis for the model development, it is assumed that the refrigerant mass flow rate is equally distributed through the number of similar compressors considered. In that case, without loss of generality, is is sufficient to mathematically describe one compression device, with Eqs. (5.1) to (5.3) providing the strategy to obtain refrigerant thermodynamic conditions at inlet and outlet of the set of compressors.

$$\dot{m}_{rf} = \dot{m}_{rf,cp,ind} \cdot n_{cp} \tag{5.1}$$

$$\varphi_{rf,1} = \varphi_{rf,cp,ind,in} \tag{5.2}$$

$$\varphi_{rf,2} = \varphi_{rf,cp,ind,out} \tag{5.3}$$

where φ can refer to any intensive property of the refrigerant, and subscript cp, ind is associated with an individual compressor.

The total compressor power input is, then, obtained from Eq. (5.4).

$$\dot{W}_{cp} = \dot{W}_{cp,ind} \cdot n_{cp} \tag{5.4}$$

Analogously, the refrigerant mass flow rate is divided by the number of evaporators present in the system, so that equal mass flow rates pass through each heat exchanger. Similarly to the compressor, Eqs.(5.5) to (5.7) describe the refrigerant conditions at inlet and exit, with Eq. (5.8) expressing the total cooling load.

$$\dot{m}_{rf} = \dot{m}_{rf,ev,ind} \cdot n_{ev} \tag{5.5}$$

$$\varphi_{rf,6} = \varphi_{rf,ev,ind,in} \tag{5.6}$$

$$\varphi_{rf,7} = \varphi_{rf,ev,ind,out} \tag{5.7}$$

$$\dot{Q}_{ev} = \dot{Q}_{ev,ind} \cdot n_{ev} \tag{5.8}$$

With that in mind, each component of the multi-compressor multi-evaporator DX refrigeration system is further described and modeled in the following sections.

5.2.1 Condenser

In the present work, the tube-and-fin condenser modeling from the Oak Ridge National Laboratory (ORNL) Heat Pump Design Model [89] was updated in regard to properties calculation, heat transfer coefficient and pressure drop correlations, as well as refrigerant charge assessment. Further, the inclusion of different types of fins and tube internal surfaces was also carried out, in order to obtain a more realistic model.

The ORNL Heat Pump Design Model is a Fortran-based computer program developed to predict the steady-state performance of conventional, vapor compression, electrically-driven, air-to-air heat pumps, operating in both heating and cooling modes [89]. The version here considered as a starting point evolved from models developed at the Oak Ridge National Laboratory [86,137] and at the Massachussettes Institute of Technology (MIT) [85], employing routines by Kartsounes and Erth [138], Flower [139], and Kusuda [140].

According to Fischer and Rice [89], the ORNL Heat Pump Design Model assumes a condenser consisting of equivalent parallel refrigerant circuits with unmixed flow on both the air and refrigerant sides, with calculations separated for the superheated, two-phase and subcooled zones of the heat exchanger. The air-side and refrigerant-side mass flow rates are divided by the number of circuits, which is a parameter that can be entered by the user, to determine values for each circuit.

The three-zone approach is developed following the structure illustrated in Figure 5.2, adapted from Martins Costa and Parise [141]. As it can be observed, the air stream is split into all three zones, with mass flow rate proportional to each zone area.

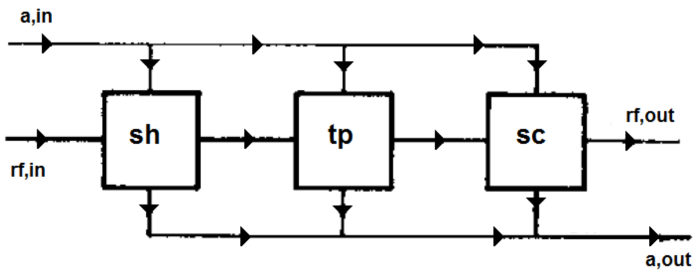

Figure 5.2: Schematic flow diagram for the multizone method applied to the condenser, adapted from Martins Costa and Parise [141].

The condenser submodel uses the physical description of the heat exchanger, the refrigerant mass flow rate, the condenser inlet air temperature and relative humidity, and the refrigerant state at the condenser inlet to evaluate the refrigerant state at the condenser outlet. A flow chart outlining the structure and the iterating processes considered for the condenser model is presented in Figure 5.3.

The following modifications were applied to the ORNL Heat Pump Design Model:

- Updated correlations for refrigerant properties, including non-azeotropic mixtures;
- Updated correlations for air properties;
- Updated correlations for refrigerant-side single-phase and two-phase heat transfer coefficients;
- Updated correlations for air-side heat transfer coefficient;
- Updated correlations for refrigerant-side single-phase and two-phase pressure drops;
- Updated models for refrigerant charge calculation;
- More options for tube internal surface;
- More options for air-side fin geometry.

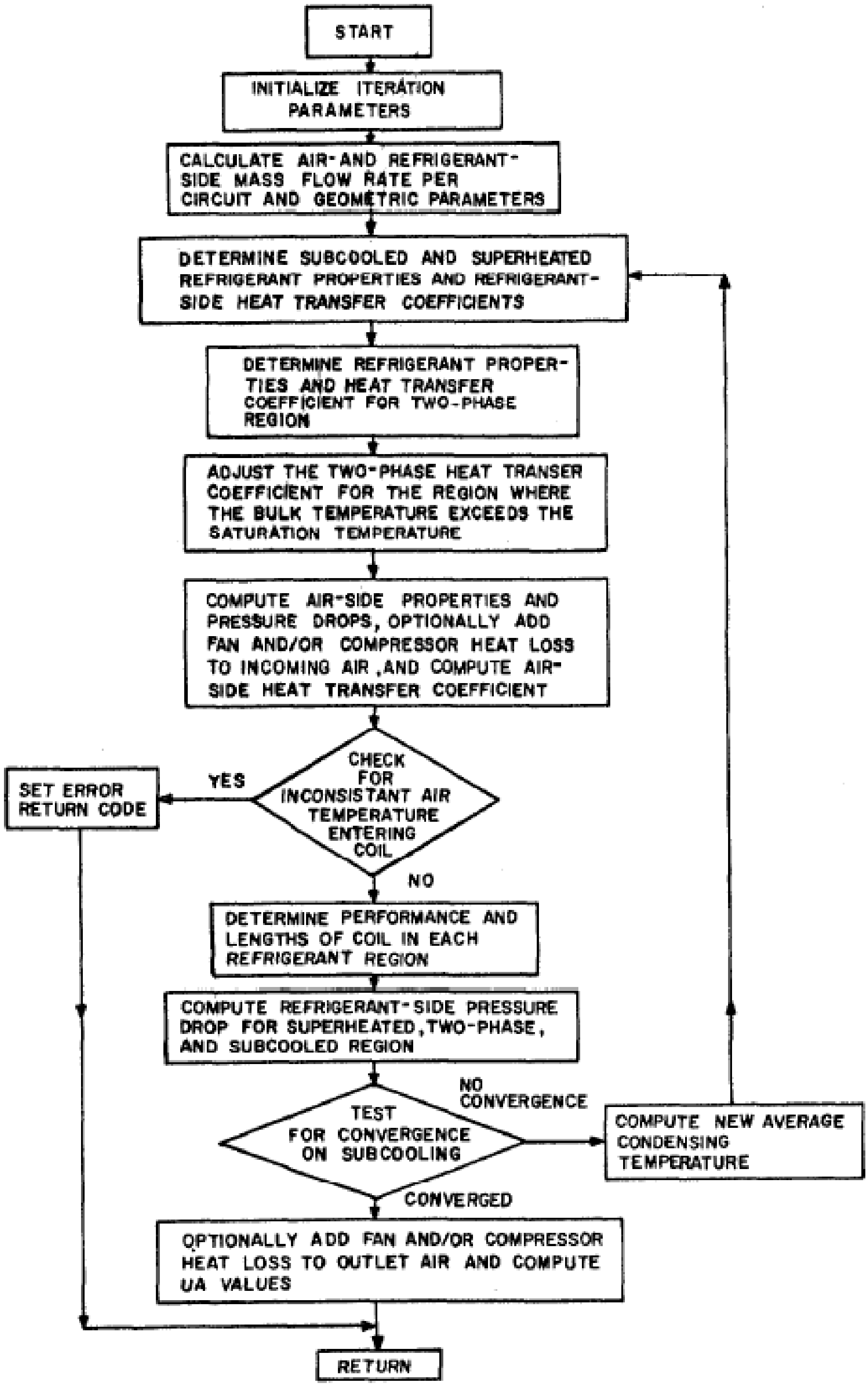

Figure 5.3: Structure and organization of the condenser from the ORNL Heat Pump Design Model [89].

The mathematical description of the updated condenser model is outlined in the following sections, from the physical definition of the tube-and-fin heat exchanger to performance calculations.

5.2.1.1
Heat exchanger geometric parameters

The physical parameters required to fully describe the condenser are listed below. All other geometry-related variables can be further calculated based on these input characteristics. The remainder of this section is devoted to explain how to compute them. Figure 5.4 provides an illustration of the tube-and-fin heat condenser, with dimensions of interest indicated [142].

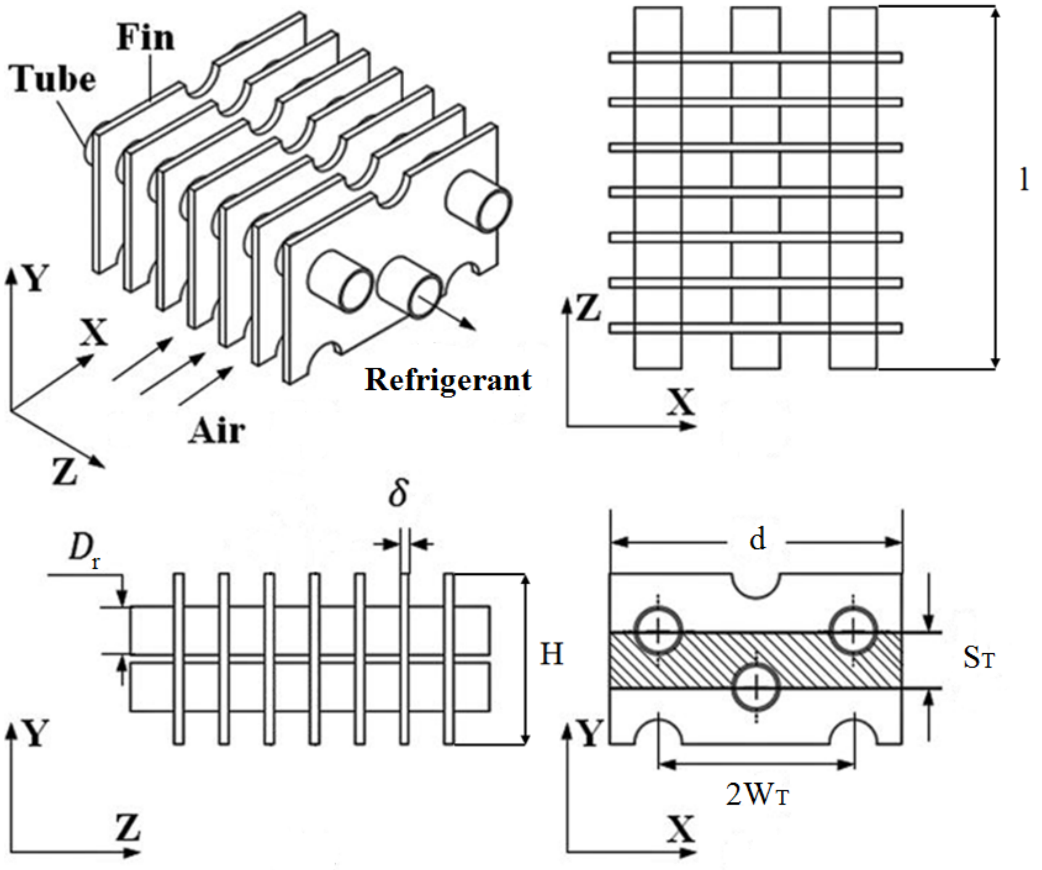

Figure 5.4: Sample tube-and-fin heat exchanger, adapted from Zhou et al. [142]).

- heat exchanger cross-sectional area, A_c;
- tube outer diameter (air-side), D_a;
- tube inner diameter (refrigerant-side), D_{rf};
- fin pitch, F_P;

- number of equivalent, parallel refrigerant circuits, N_{circ};
- number of tube rows in transverse direction, N_T;
- tubes transverse pitch, S_T;
- tubes longitudinal pitch, W_T; and
- fin thickness, δ.

The total number of refrigerant tubes, N_{tot}, as well as the depth, d, and height, H, of the heat exchanger are computed as follows:

$$N_{tot} = N_V N_T \tag{5.9}$$

$$d = N_T W_T \tag{5.10}$$

$$H = N_V S_T \tag{5.11}$$

The lenght of the heat exchanger, l, is determined next:

$$l = \frac{A_c}{N_V S_T} \tag{5.12}$$

The number of fins, N_f, is defined by Eq.(5.13).

$$N_f = \frac{A_c F_P}{N_V S_T} \tag{5.13}$$

The length of each tube not covered by fins, l_{exp}, and the "projected" area of tubes obstructing air flow, A^*_{tub}, can be written as, respectively:

$$l_{exp} = \frac{A_c}{N_V S_T}\left(1 - F_P \delta\right) \tag{5.14}$$

$$A^*_{tub} = \frac{A_c D_a}{S_T}\left(1 - F_P \delta\right) \tag{5.15}$$

The air-side heat transfer area, A_a, is calculated in Eq.(5.16), whilst Eq.(5.17) describes the refrigerant-side heat transfer area, A_{rf}.

$$A_a = \frac{N_T A_c}{S_T}\left[2F_P\left(S_T W_T - \frac{\pi D_a^2}{4}\right) + \pi D_a\right] \tag{5.16}$$

$$A_{rf} = \frac{N_T A_c \pi D_{rf}}{S_T} \tag{5.17}$$

The total cross-sectional area of the fins obstructing air-flow, A^*_f, is defined by Eq.(5.18), so that the minimum free-flow frontal area, A_{ff}, is represented in Eq.(5.19).

$$A^*_f = A_c F_P \delta \tag{5.18}$$

$$A_{ff} = \frac{A_c}{S_T}\left(S_T - D_a\right)\left(1 - F_P \delta\right) \tag{5.19}$$

Eq.(5.20) describes the refrigerant-side heat transfer area per unit of number of parallel circuits, A_{rh}, while the refrigerant-side heat transfer area per unit of mass flow rate of air, a_0, is defined by Eq.(5.21):

$$A_{rh} = \frac{N_T A_c \pi D_{rf}}{S_T N_{circ}} \tag{5.20}$$

$$a_0 = \frac{N_T \pi D_{rf}}{G_a \left(S_T - D_a\right)\left(1 - F_P \delta\right)} \tag{5.21}$$

Now, considering σ_a as the ratio between free-flow frontal area and frontal area,

$$\sigma_a = \frac{\left(S_T - D_a\right)\left(1 - F_P \delta\right)}{S_T}, \tag{5.22}$$

parameter a_0 can be rewritten as:

$$a_0 = \frac{N_T \pi D_{rf}}{G_a \sigma_a S_T} \tag{5.23}$$

The ratio between air-side heat transfer area and minimum free-flow frontal area, a^*_{min}, is determined by Eq.(5.24).

$$a^*_{min} = \frac{A_a}{A_{ff}} \tag{5.24}$$

Regarding the tube internal surface, three different types can be selected for the heat exchanger: smooth, micro-finned or cross-grooved tube. Micro-finned tubes were first developed by Fuji et al. [143] of Hitachi Cable Ltd, and described by Tatsumi et al. [144]. Later, design variants, cross-grooved surfaces being one of them, were defined by Shinohara and Tobe [145]. Additionally, Webb [146] thoroughly described their historical development and performance for condensation and evaporation processes [147].

When an enhanced tube surface, either micro-finned or cross-grooved, is considered, additional geometric parameters must be defined to fully describe the heat exchanger. They are the following:

- fin angle, γ_1;
- helix angle, γ_2;
- fin height, γ_3;
- number of fins , γ_4.

Figure 5.5 illustrates the geometry of micro-finned and cross-grooved tubes, based on Cavallini et al. [148].

For the air-side fin geometry, four options are present: flat, wavy, louvered or lanced fin. The first successful heat transfer and friction factor correlations for flat fin geometry were proposed by McQuiston [149]. Wang et al. [150] thoroughly studied the heat exchange and pressure drop in tube-and-fin heat

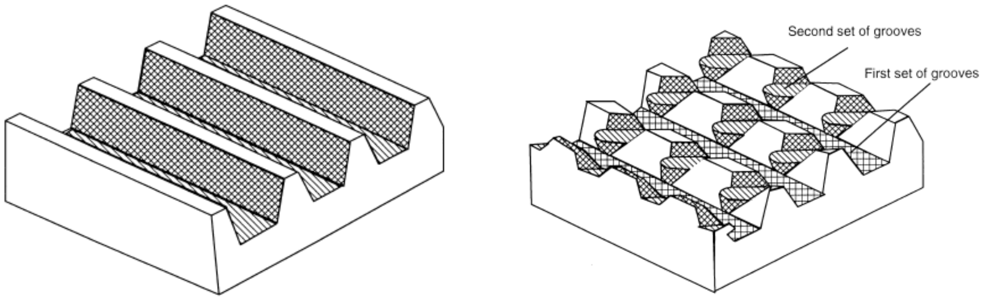

5.5(a): Micro-finned tube

5.5(b): Cross-grooved tube

Figure 5.5: Typical configuration of enhanced internal surfaces: micro-finned and cross-grooved tubes (based on Cavallini et al. [148]).

exchangers with flat fin. Enhanced fins can, however, significantly improve the heat transfer in comparison with their plain fin counterpart. Wang et al. [151]–[153] constructed correlations for the air-side performance and friction of tube-and-fin heat exchangers with wavy, louvered and lanced fin patterns, based on consistent reduction methods.

If wavy fins are selected, the following options for corrugation angle, as addressed by Wang et al. [151], are available: 9.76, 10.76 or 11.76°.

When a fin of the louvered pattern is chosen, the louver angle must be defined among (Wang et al. [152]) 13.50, 24.47, 24.89, 25.00, 28.15, 30.24 or 39.45 °.

For a tube-and-fin heat exchanger with lanced fins, one of the three options that follow, which are further described in Wang et al. [153], can be selected: slit-medium, superslit-low or superslit-high.

Figure 5.6 shows the geometry of wavy and louvered fin-and-tube heat exchangers, adapted from Wang et al. [151, 152]. Corrugation angle, for wavy fins, and louver angles, for louvered fins, are schematically represented in Figure 5.7.

5.2.1.2
Heat exchanger thermal performance

The performance of the condenser is calculated by means of the computational sequence illustrated in Figure 5.8 [89].

According to Fischer and Rice [89], effectiveness-NTU correlations are used to compute the heat transfer for the single-phase and two-phase refrigerant regions of the heat exchanger. Eqs.(5.25) and (5.26) give the number of transfer units and the effectiveness, respectively, for the two-phase region of the condenser.

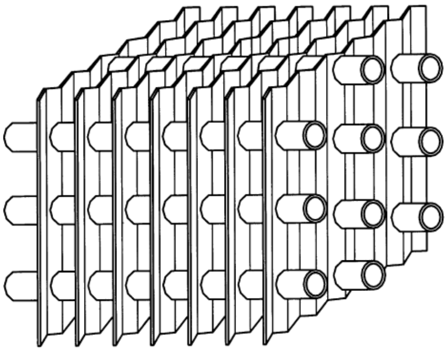

5.6(a): Wavy fin

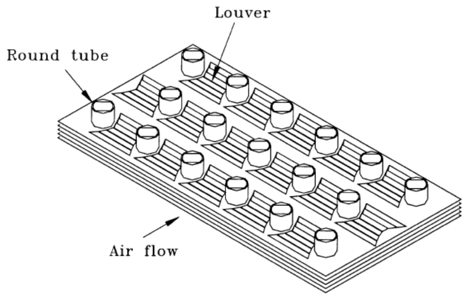

5.6(b): Louvered fin

Figure 5.6: Schematic of typical fin patterns for tube-and-fin heat exchangers: wavy and louvered fins (adapted from Wang et al. [151, 152])

.

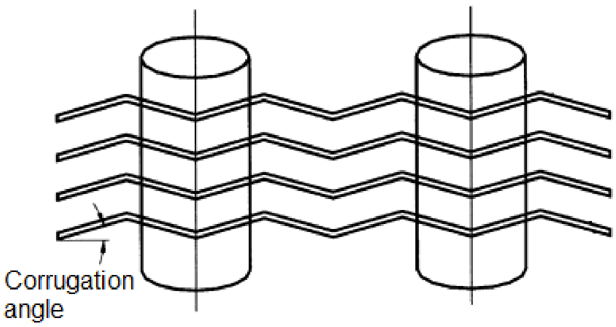

5.7(a): Corrugation angle of a wavy fin

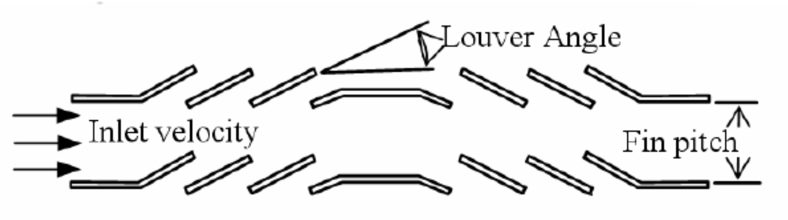

5.7(b): Louver angle of a louvered fin

Figure 5.7: Representation of fin angles for wavy and louvered tube-and-fin heat exchangers: corrugation and louver angles (adapted from Wang et al. [151] and Vorayos and Kiatsiriroat [154], respectively)

.

$$NTU_{tp} = \frac{UA}{C_{min,tp}} = \frac{a_0}{c_{p,m}\left(\dfrac{A_{rf}}{\eta_d \alpha_a A_a} + \dfrac{1}{\alpha_{rf,tp}}\right)} \tag{5.25}$$

$$\varepsilon_{tp} = 1 - \exp\left(-NTU_{tp}\right) \tag{5.26}$$

where a_0 is the refrigerant-side heat transfer area per unit of air mass flow rate, defined in Eq.(5.21), and U is the overall heat transfer coefficient, based on Eq(5.27), with η_d representing the air-side finned area effectiveness.

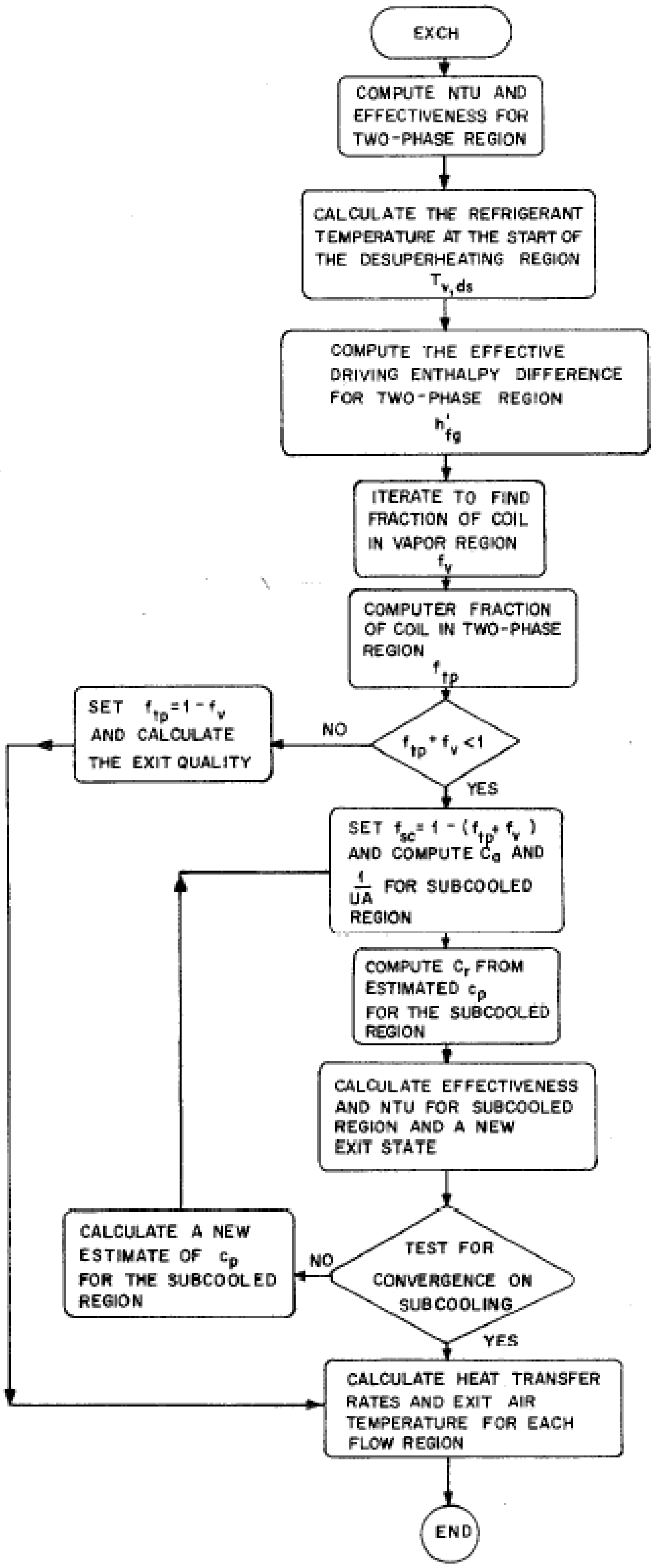

Figure 5.8: Block diagram for the condenser performance calculation, adapted from the ORNL Heat Pump Design Model [89].

$$\frac{1}{UA} = \frac{1}{\eta_d \alpha_a A_a} + \frac{1}{\alpha_{rf,tp} A_{rf}} \tag{5.27}$$

In order to further calculate the pressure drop and the heat transfer rate for the two-phase, superheat, and subcooled regions, it is necessary to determine the fraction of each coil. From Fischer and Rice [89], for the fraction (in relation of heat exchanger area occupied by each zone) of the condenser consisting of two-phase refrigerant, the heat transfer rate required to fully condense the refrigerant flow, $\dot{Q}_{tp}$, is considered, as expressed by Eq. (5.28).

$$\dot{Q}_{tp} = \dot{m}_{rf} h'_{rf,fg} \tag{5.28}$$

where the so-called effective driving enthalpy difference in the two-phase region, h'_{fg}, can be determined with Eqs.(5.29) and (5.30) [89], with h_{fg} representing the refrigerant latent heat.

$$h'_{fg} = h_{fg} + c_{p,rf,v} \left(T^*_{v,ds} - T_{rf,v} \right) \tag{5.29}$$

$$h_{fg} = h_{rf,v} - h_{rf,l} \tag{5.30}$$

The bulk refrigerant temperature at the end of the single-phase vapor region, that is, at which refrigeration condensation begins at the tube wall, $T_{v,ds}$, is obtained from Eq.(5.31) [89].

$$T_{v,ds} = \frac{\psi T_{rf,v} - T_{a,in}}{r - 1} \tag{5.31}$$

where $T_{rf,v}$ represents the refrigerant temperature entering the two-phase region, $T_{a,in}$, the inlet air temperature, and ψ, a paremeter given by (5.32).

$$\psi = 1 + \frac{\alpha_v A_{rf}}{\alpha_a A_a \eta_d} \tag{5.32}$$

Eqs.(5.33) and (5.34) describe, respectively, the mass flow rate of air required to achieve $\dot{Q}_{tp}$ and the fraction of the coil containing two-phase refrigerant.

$$\dot{m}_{a,tp} = \frac{\dot{Q}_{tp}}{\varepsilon_{tp} c_{p,m} \left| T_{rf,tp,avg} - T_{a,in} \right|} \tag{5.33}$$

$$f_{tp} = \frac{\dot{m}_{a,tp}}{\dot{m}_a} \tag{5.34}$$

Further, according to Fischer and Rice [89], in case the sum $f_{tp} + f_v$ is greater than 1, then f_{tp} is set as $1 - f_v$. The number of transfer units for the subcooled and superheated regions of the condenser are given, respectively, by Eqs.(5.35) and (5.36).

$$NTU_l = \frac{1}{R_l C_{min,l}} \tag{5.35}$$

$$NTU_v = \frac{1}{R_v C_{min,v}} \tag{5.36}$$

where the thermal resistances, R_l and R_v are obtained with Eqs.(5.37) and (5.38). Conduction thermal resistances are, given the small magnitude of their contribution, neglected [89].

$$R_l = \frac{1}{f_l A_{rh}} \left(\frac{A_{rf}}{\eta_d \alpha_a A_a} + \frac{1}{\alpha_{rf,l}} \right) \tag{5.37}$$

$$R_v = \frac{1}{f_v A_{rh}} \left(\frac{A_{rf}}{\eta_d \alpha_a A_a} + \frac{1}{\alpha_{rf,v}} \right) \tag{5.38}$$

Regarding the effectiveness of the subcooled and superheated regions, an approximate solution, developed by Hiller and Glicksman [85], is considered. Such approximation assumes a cross-flow heat exchanger with both fluids unmixed. In that sense, Eqs.(5.39) and (5.40) are associated with a counterflow heat exchanger, whilst the correction for a cross-flow orientation is obtained with Eqs.(5.41) and (5.42).

$$\varepsilon_{cf,l} = \begin{cases} \dfrac{1 - \exp -NTU_l \left(1 - \dfrac{C_{min,l}}{C_{max,l}}\right)}{\left(1 - \dfrac{C_{min,l}}{C_{max,l}}\right) \exp -NTU_l \left(1 - \dfrac{C_{min,l}}{C_{max,l}}\right)} & \text{if } C_{min,l} < C_{max,l}; \\ \\ \dfrac{NTU_l}{1 + NTU_l} & \text{if } C_{min,l} = C_{max,l}. \end{cases} \tag{5.39}$$

$$\varepsilon_{cf,v} = \begin{cases} \dfrac{1 - \exp[-NTU_v \left(1 - \dfrac{C_{min,v}}{C_{max,v}}\right)]}{\left(1 - \dfrac{C_{min,v}}{C_{max,v}}\right) \exp -NTU_v \left(1 - \dfrac{C_{min,v}}{C_{max,v}}\right)} & \text{if } C_{min,v} < C_{max,v}; \\ \\ \dfrac{NTU_v}{1 + NTU_v} & \text{if } C_{min,v} = C_{max,v}. \end{cases} \tag{5.40}$$

$$\varepsilon_l = \varepsilon_{cf,l} \frac{1}{\dfrac{C_{min,l}}{C_{max,l}} \left(1 + 0.047 \dfrac{C_{min,l}}{C_{max,l}}\right) (NTU_l)^{0.036}} \tag{5.41}$$

$$\varepsilon_v = \varepsilon_{cf,v} \frac{1}{\dfrac{C_{min,v}}{C_{max,v}} \left(1 + 0.047 \dfrac{C_{min,v}}{C_{max,v}}\right) (NTU_v)^{0.036}} \tag{5.42}$$

Since all three refrigerant regions can be present in the condenser, determining the fraction of the heat exchanger which is superheated, f_v, requires two iterations: first on f_v, and then on C_{max}/C_{min}, until Eq.(5.43), relating maximum to actual heat transfer transfer rate with the zone effectiveness, which is a function of capacity rates ratio and NTU, is satisfied [89].

$$\frac{C_{max,v}\left|T_{in}-T_{out}\right|_{max}}{C_{min,v}\left(T_{rf,in}-T_{a,in}\right)}=\varepsilon_v\left(\frac{C_{max,v}}{C_{min,v}},NTU_v\right) \tag{5.43}$$

where

$$C_{a,v}=\dot{m}_a c_{p,m} f_v = C_{min,v} \text{ or } C_{max,v} \tag{5.44}$$

Thus, in case there is subcooled liquid at the condenser exit, the fraction of the heat exchanger which is subcooled, f_l, can be determined considering the values of f_{tp} and f_v previously calculated.

$$f_l = 1 - f_{tp} - f_v \tag{5.45}$$

with $C_{a,l}$ calculated analousgy as in Eq.(5.44), that is:

$$C_{a,l}=\dot{m}_a c_{p,m} f_l = C_{min,l} \text{ or } C_{max,l} \tag{5.46}$$

The heat transfer rate and the effectiveness associated to the subcooled region of the condenser can, according to Fischer and Rice [89], be determined by iterating on the exit temperature and the average specific heat for the liquid refrigerant. Such condition is due to the dependency of the refrigerant capacity rate, $C_{rf,l}$, on the average refrigerant specific heat for the subcooled region, and thus on the exit temperature.

Regarding the heat transfer for the entire coil, it is defined as the sum of the rates for the two-phase region, computed using Eq.(5.28) and the rates for the subcooled and superheated regions, calculated in accordance with Eqs.(5.47) and (5.48) [89].

$$\dot{Q}_l = C_{rf,l}\Delta T_{rf,l} \tag{5.47}$$

$$\dot{Q}_v = C_{rf,v}\Delta T_{rf,v} \tag{5.48}$$

where

$$C_{rf,l} = \dot{m}_{rf} c_{p,rf,l} \tag{5.49}$$

$$C_{rf,v} = \dot{m}_{rf} c_{p,rf,v} \tag{5.50}$$

Therefore,

$$\dot{Q} = \dot{Q}_{tp} + \dot{Q}_l + \dot{Q}_v \tag{5.51}$$

Further, Eqs.(5.52) to (5.54) are applied to compute the air-side temperature change for each of the three regions.

$$\Delta T_{a,tp} = \frac{\dot{Q}_{tp}}{C_{a,tp}} \tag{5.52}$$

$$\Delta T_{a,v} = \frac{\dot{Q}_{v}}{C_{a,v}} \tag{5.53}$$

$$\Delta T_{a,l} = \frac{\dot{Q}_l}{C_{a,l}} \tag{5.54}$$

where $\dot{Q}_{tp}$, $\dot{Q}_v$, $\dot{Q}_l$ are variables associated to air-side sensible heat transfer alone, and $C_{a,tp}$ is defined analousgy to Eq.(5.44).

$$C_{a,tp} = \dot{m}_{a,tp} c_{p,m} \tag{5.55}$$

Finally, the average air temperature at the exit of the condenser can be determined with Eq.(5.56) [89].

$$T_{a,out} = T_{a,in} + \frac{\dot{Q}_{tp} + \dot{Q}_v + \dot{Q}_l}{\dot{m}_a c_{p,m}} \tag{5.56}$$

5.2.1.3
Refrigerant-side single-phase heat transfer coefficient

The refrigerant single-phase heat transfer coefficient in the condenser tubes is calculated for three different types of internal surfaces: smooth, micro-finned and cross-grooved. When fully developed laminar flow is considered, regardless of the internal surface of the tube, heat transfer coefficient can be derived from first principles [155]. For predicting fully developed turbulent flow heat transfer coefficient inside smooth tubes, the Dittus-Boelter correlation [156] is applied. In the case of turbulent flow through micro-finned or cross-groved tubes, Huang [157], who modeled air-conditioning condensers and evaporators with emphasis on in-tube enhancement, presented enhancement factors based on the Dittus-Boelter correlation as a function of Reynolds number only.

The refrigerant heat transfer coefficient in the superheated region of the condenser is calculated by Eq.(5.57) [157].

$$Nu_{rf,v} = \begin{cases} 4.364 & \text{if } Re_{rf,v} < 2300; \\ 0.023\ Pr_{rf,v}^{0.4} Re_{rf,v}^{0.8} & \text{if } Re_{rf,v} \geq 2300 \text{ and smooth;} \\ 0.023\ E_h\ Pr_{rf,v}^{0.4} Re_{rf,v}^{0.8} & \text{if } Re_{rf,v} \geq 2300 \text{ and enhanced;} \end{cases} \tag{5.57}$$

where

$$Nu_{rf,v} = \frac{\alpha_{rf,v} D_{rf}}{k_{rf,v}} \tag{5.58}$$

$$Re_{rf,v} = \frac{D_{rf} G_{rf}}{\mu_{rf,v}} \tag{5.59}$$

$$Pr_{rf,v} = \frac{\mu_{rf,v} c_{p,rf,v}}{k_{rf,v}} \tag{5.60}$$

The refrigerant mass flux, G_{rf}, is calculated by

$$G_{rf} = \frac{\dot{m}_{rf}}{\frac{\pi D_{rf}^2}{4}} \tag{5.61}$$

where, even for enhanced surfaces like micro-finned and cross-grooved tubes, the cross-sectional area is referred to as in (5.61).

Likewise, the refrigerant heat transfer coefficient in the subcooled region of the condenser is computed using Eq. (5.62) [157].

$$Nu_{rf,l} = \begin{cases} 4.364 & \text{if } Re_{rf,l} < 2300; \\ 0.023\ Pr_{rf,l}^{0.4} Re_{rf,l}^{0.8} & \text{if } Re_{rf,l} \geq 2300 \text{ and smooth;} \\ 0.023\ E_h\ Pr_{rf,l}^{0.4} Re_{rf,l}^{0.8} & \text{if } Re_{rf,l} \geq 2300 \text{ and enhanced;} \end{cases} \tag{5.62}$$

where

$$Nu_{rf,l} = \frac{\alpha_{rf,l} D_{rf}}{k_{rf,l}} \tag{5.63}$$

$$Re_{rf,l} = \frac{D_{rf} G_{rf}}{\mu_{rf,l}} \tag{5.64}$$

$$Pr_{rf,l} = \frac{\mu_{rf,l} c_{p,rf,l}}{k_{rf,l}} \tag{5.65}$$

The enhancement factor, E_h, for micro-finned or cross-grooved internal surfaces, valid for both liquid and vapor, is determined as follows [157]:

$$E_h = 1.7622 - 8.778 \cdot 10^{-5} Re_{rf} + 5.5556 \cdot 10^{-9} Re_{rf}^2 \tag{5.66}$$

5.2.1.4 Refrigerant-side two-phase heat transfer coefficient

The refrigerant heat transfer coefficient in forced convection condensation inside tubes is calculated by Eq.(5.67), based on Cavallini et al. [158]. This correlation was selected due to its good agreement with a set of experimental data composed of condensation for single fluids (R22, R32, R134a,R125), azeotropic mixtures (R410A, R502, R507A) and zeotropic mixtures (R407C, R32/R125 and R32/R134a), including two new very low GWP refrigerants (HFO-1234yf and HFO-1234ze) [159].

$$\alpha_{tp}^* = Nu_{rf} \left(\frac{k_{rf,l}}{D_{rf}^*} \right) \tag{5.67}$$

where

$$Nu = 0.05\ Re_{rf,eq}^{0.8}\ Pr_{rf,l}^{0.33}\ Rx^{\gamma_1} \left(Bo_{rf} Fr_{rf}\right)^{\gamma_2} \tag{5.68}$$

Exponents γ_1 and γ_2 are computed for different types of internal tube surfaces, as follows:

$$\gamma_1 = \begin{cases} 0 & \text{if smooth;} \\ 1.4 & \text{if micro-finned and } \beta_3/D_r \geq 0.04; \\ 2.0 & \text{if micro-finned and } \beta_3/D_r < 0.04; \\ 2.1 & \text{if cross-grooved.} \end{cases} \tag{5.69}$$

$$\gamma_2 = \begin{cases} 0 & \text{if smooth;} \\ -0.08 & \text{if micro-finned and } \beta_3/D_r \geq 0.04; \\ -0.26 & \text{if micro-finned and } \beta_3/D_r < 0.04; \\ -0.26 & \text{if cross-grooved.} \end{cases} \tag{5.70}$$

A paremeter, D^*_{rf}, is defined as an adjustment of D_{rf}, considering, once again, the distinct types of surfaces, as outlined in Eq.(5.71).

$$D^*_{rf} = \sqrt{\frac{4A_{sec}}{\pi}} \tag{5.71}$$

where

$$A_{sec} = \begin{cases} \dfrac{\pi D_{rf}^2}{4} & \text{if smooth;} \\ \dfrac{\pi D_{rf}^2}{4} - \beta_4 A_{fin} & \text{if enhanced.} \end{cases} \tag{5.72}$$

and

$$A_{fin} = tan\left(\frac{\beta_1}{2}\right)\frac{\beta_2^3}{cos\left(\beta_2\right)} \tag{5.73}$$

The refrigerant equivalent Reynolds number, $Re_{rf,eq}$, is computed by means of the superficial vapor and superficial liquid Reynolds numbers, $Re^*_{rf,v}$ and $Re^*_{rf,l}$, respectively [158].

$$Re_{rf,eq} = Re^*_{rf,l} + Re^*_{rf,v}\left(\frac{\mu_{rf,v}}{\mu_{rf,l}}\right)\left(\frac{\rho_{rf,l}}{\rho_{rf,v}}\right)^{0.5} \tag{5.74}$$

where

$$Re^*_v = \frac{G^*_{rf} x_{qw} D^*_{rf}}{\mu_v} \tag{5.75}$$

$$Re^*_l = \frac{G^*_{rf}\left(1 - x_{qw}\right) D^*_{rf}}{\mu_l} \tag{5.76}$$

and x_{qw} is the average vapor quality, calculated as the arithmetic mean between the inlet and outlet quality values.

The refrigerant mass flux adjusted for enhanced surfaces, G^*_{rf}, defined by Cavallini et al. [158], is calculated as follows:

$$G^*_{rf} = \frac{\dot{m}_{rf}}{A_{sec}} \tag{5.77}$$

Parameter Rx, as well as the refrigerant Bond and Froude numbers, are computed by Eqs.(5.78), (5.79) and (5.80), respectively.

$$Rx = \begin{cases} 1 & \text{if smooth;} \\ \\ \dfrac{2\beta_3\beta_4\left[1 - sin\left(\dfrac{\beta_1}{2}\right)\right] cos\left(\beta_2\right)}{\left[\pi D^*_{rf} cos\left(\dfrac{\beta_1}{2}\right)\right] + 1} & \text{if enhanced.} \end{cases} \tag{5.78}$$

$$Bo = \begin{cases} 1 & \text{if smooth;} \\ \\ \dfrac{9.18\rho_l\beta_3\pi D^*_{rf}}{8\sigma_{rf}\beta_4} & \text{if enhanced.} \end{cases} \tag{5.79}$$

$$Fr = \begin{cases} 1 & \text{if smooth;} \\ \\ \dfrac{\left(\dfrac{G^*_{rf}}{\rho_{rf,v}}\right)^2}{9.18D^*_{rf}} & \text{if enhanced.} \end{cases} \tag{5.80}$$

where σ_{rf} is the surface tension obtained considering refrigerant average pressure and bulk enthalpy, at saturated liquid condition, as below:

$$\sigma_{rf} = f\left(P_{rf,avg}, h_{rf,l}\right) \tag{5.81}$$

Finally, when the average quality value is not between 0.1 and 0.95, Cavallini et al. [158] suggested an interpolation method for evaluating the heat transfer coefficient, as presented in Eq.(5.82):

$$\alpha_{tp} = \begin{cases} \dfrac{\left(0.1 - x_{qw}\right)\alpha_{rf,l} + x_{qw}\alpha^*_{rf,tp}}{0.1} & \text{if } x_{qw} < 0.1; \\ \\ \alpha^*_{rf,tp} & \text{if } 0.1 \leq x_{qw} \leq 0.95; \\ \\ \dfrac{\left(x_{qw} - 0.95\right)\alpha_{rf,v} + \left(1 - x_{qw}\right)\alpha^*_{rf,tp}}{0.05} & \text{if } x_{qw} > 0.95. \end{cases} \tag{5.82}$$

5.2.1.5
Air-side heat transfer coefficient

The heat transfer coefficient for the air-side of the condenser is based on the work of Wang et al. [150–153], who studied and proposed correlations for the air-side performance of flat, wavy, louvered and lanced fin-and-tube heat exchangers, based on consistent reduction methods.

The air-side heat transfer characteristics are presented in terms of the Colburn factor, j:

$$\alpha_a = j\ G_a\ c_{p,a}\ Pr_a^{-2/3} \tag{5.83}$$

where G_a and Pr_a represent, respectively, the mass flux of air based on the minimum flow area and the air Prandtl number, calculated as:

$$G_a = V_{a,max}\rho_{a,in} \tag{5.84}$$

$$Pr_a = \frac{\mu_a c_{p,m}}{k_a} \tag{5.85}$$

where $c_{p,m}$ is the specific heat for moist air conditions, obtained in terms of the air humidity ratio, w, as follows:

$$c_{p,m} = \frac{c_{p,a} + 1.805w}{1 + w} \tag{5.86}$$

The maximum velocity inside the heat exchanger, $V_{a,max}$, is computed in terms of the minimum free-flow frontal area and the air flow rate, as expressed in Eq.(5.87).

$$V_{a,max} = \frac{\dot{V}_a}{A_{ff}} \tag{5.87}$$

The final equation forms for the j factors are given according to the type of fin considered, as summarized by Eq.(5.88). These expressions are dependent on a number of parameters, including the hydraulic diameter, D_h, and the fin collar outside diameter, D_c, defined by Eqs.(5.89) and (5.90), respectively.

$$j = \begin{cases} j_{fl} & \text{if flat;} \\ j_{wv} & \text{if wavy;} \\ j_{lv} & \text{if louvered;} \\ j_{lc} & \text{if lanced.} \end{cases} \tag{5.88}$$

$$D_h = \frac{4N_T W_T}{a^*_{min}} \tag{5.89}$$

$$D_c = D_a + 2\delta \tag{5.90}$$

Flat fins. For a flat fin-and-tube heat exchanger, Eq.(5.91) is considered for the determination of the Colburn factor, as reported by Wang et al. [150].

$$j_{fl} = \begin{cases} 0.108\ Re_{a,D_c}^{-0.29} \left(\frac{S_T}{W_T}\right)^{\lambda_1} \left(\frac{F_P{}^{-1}}{D_c}\right)^{-1.084} \left(\frac{F_P{}^{-1}}{D_h}\right)^{-0.786} \left(\frac{F_P{}^{-1}}{S_T}\right)^{\lambda_2} & \text{if } N_T = 1; \\ 0.086\ Re_{a,D_c}^{\lambda_3}\ N_T{}^{\lambda_4} \left(\frac{F_P{}^{-1}}{D_c}\right)^{\lambda_5} \left(\frac{F_P{}^{-1}}{D_h}\right)^{\lambda_6} \left(\frac{F_P{}^{-1}}{S_T}\right)^{-0.93} & \text{if } N_T \geq 2. \end{cases} \tag{5.91}$$

where

$$\lambda_1 = 1.9 - 0.23 \log_e \left(Re_{a,D_c}\right) \tag{5.92}$$

$$\lambda_2 = -0.236 + 0.126 \log_e \left(Re_{a,D_c}\right) \tag{5.93}$$

$$\lambda_3 = -0.361 - \frac{0.042 N_T}{\log_e \left(Re_{a,D_c}\right)} + 0.158 \log_e \left[N_T \left(\frac{F_P{}^{-1}}{D_c}\right)^{0.41}\right] \tag{5.94}$$

$$\lambda_4 = -1.224 - \frac{0.076 \left(\frac{W_T}{D_h}\right)^{1.42}}{\log_e \left(Re_{a,D_c}\right)} \tag{5.95}$$

$$\lambda_5 = -0.083 + \frac{0.058 N_T}{\log_e \left(Re_{a,D_c}\right)} \tag{5.96}$$

$$\lambda_6 = -5.735 + 1.21 \log_e \left(\frac{Re_{a,D_c}}{N_T}\right) \tag{5.97}$$

Wavy fins. If wavy fins were present, Wang et al. [151] suggested the following expression:

$$j_{wv} = 0.324\ Re_{a,D_c}^{\lambda_1} \left(\frac{F_P^{-1}}{W_T}\right)^{\lambda_2} (\tan\theta)^{\lambda_3} \left(\frac{W_T}{S_T}\right)^{\lambda_4} N_T^{0.428} \tag{5.98}$$

where θ can vary between 9.76, 10.76 and 11.76°.

In such case,

$$\lambda_1 = -0.229 + 0.115 \left(\frac{F_P^{-1}}{D_c}\right)^{0.6} \left(\frac{W_T}{D_h}\right)^{0.54} N_T^{-0.284} \log_e \left(0.5 \tan\theta\right) \tag{5.99}$$

$$\lambda_2 = -0.251 + \frac{0.232\ N_T^{1.37}}{\log_e \left(Re_{a,D_c}\right) - 2.303} \tag{5.100}$$

$$\lambda_3 = -0.439 \left(\frac{F_P^{-1}}{D_h}\right)^{0.09} \left(\frac{W_T}{S_T}\right)^{-1.75} N_T^{-0.93} \tag{5.101}$$

$$\lambda_4 = 0.502 \left[\log_e \left(Re_{a,D_c}\right) - 2.54\right] \tag{5.102}$$

For a wavy fin-and-tube heat exchanger, the minimum free-flow frontal area is calculated by Eq.(5.103), below, instead of Eq.(5.19) [151].

$$A_{ff} = \frac{A_c}{S_T}\left(S_T - D_a\right)\left(1 - \frac{F_P}{\cos\theta}\delta\right) \tag{5.103}$$

Louvered fins. When a heat exchanger with fins of the louvered type is considered, the correlation presented by Wang et al. [152] is the following:

$$j_{lv} = \begin{cases} 14.3117\ Re_{a,D_c}^{\lambda_1}\left(\dfrac{F_P^{-1}}{D_c}\right)^{\lambda_2}\Omega^{\lambda_3}\left(\dfrac{F_P^{-1}}{W_T}\right)^{\lambda_4}\left(\dfrac{W_T}{S_T}\right)^{-1.724} & \text{if } Re_{a,D_c} < 1000; \\ \\ 1.1373\ Re_{a,D_c}^{\lambda_5}\left(\dfrac{F_P^{-1}}{W_T}\right)^{\lambda_6}\Omega^{\lambda_7}\left(\dfrac{W_T}{S_T}\right)^{\lambda_8} N_T^{0.3545} & \text{if } Re_{a,D_c} \geq 1000. \end{cases} \tag{5.104}$$

where paremeter Ω varies as follows:

$$\Omega = \begin{cases} 0.240 & \text{if } \theta = 13.50°; \\ 0.455 & \text{if } \theta = 24.47°; \\ 0.464 & \text{if } \theta = 24.89°; \\ 0.466 & \text{if } \theta = 25.00°; \\ 0.535 & \text{if } \theta = 28.15°; \\ 0.583 & \text{if } \theta = 30.24°; \\ 0.823 & \text{if } \theta = 39.45°. \end{cases} \tag{5.105}$$

In that sense,

$$\lambda_1 = -0.991 - 0.1055\left(\frac{W_T}{S_T}\right)^{3.1}\log_e\left(\Omega\right) \tag{5.106}$$

$$\lambda_2 = -0.7344 + 2.1059\left[\frac{{N_T}^{0.55}}{\log_e\left(Re_{a,D_c}\right) - 3.2}\right] \tag{5.107}$$

$$\lambda_3 = 0.08485 + \left(\frac{W_T}{S_T}\right)^{-4.4} N_T^{-0.68} \tag{5.108}$$

$$\lambda_4 = -0.1741\log_e\left(N_T\right) \tag{5.109}$$

$$\lambda_5 = -0.6027 + 0.02593\left(\frac{W_T}{D_h}\right)^{0.52} N_T^{-0.5}\log_e\left(\Omega\right) \tag{5.110}$$

$$\lambda_6 = -0.4776 + 0.40774\left[\frac{{N_T}^{0.7}}{\log_e\left(Re_{a,D_c}\right) - 4.4}\right] \tag{5.111}$$

$$\lambda_7 = -0.58655\left(\frac{F_P^{-1}}{D_h}\right)^{2.3}\left(\frac{W_T}{S_T}\right)^{-1.6} N_T^{-0.65} \tag{5.112}$$

$$\lambda_8 = 0.0814\left[\log_e\left(Re_{D_c}\right) - 3\right] \tag{5.113}$$

With louvered fins, the calculation of the minimum free-flow frontal area is represented by Eq.(5.19) [152].

Lanced fins. Eq.(5.114) is applied for lanced fin-and-tube heat exchangers, as reported by Wang et al. [153].

$$j_{lc} = \begin{cases} 1.0691\ Re_{a,D_c}^{\lambda_4} \left(\dfrac{F_P^{-1}}{D_c}\right)^{\lambda_5} \left(\dfrac{\kappa_s}{\kappa_h}\right)^{\lambda_6} N_T^{\lambda_7} & \text{if } N_T \leq 2; \\ 0.9047\ Re_{a,D_c}^{\lambda_1} \left(\dfrac{F_P^{-1}}{D_c}\right)^{\lambda_2} \left(\dfrac{S_T}{W_T}\right)^{\lambda_3} \left(\dfrac{\kappa_s}{\kappa_h}\right)^{-0.0305} N_T^{0.0782} & \text{if } N_T > 2 \text{ and } Re_{a,D_c} \leq 700; \\ 1.0691\ Re_{a,D_c}^{\lambda_4} \left(\dfrac{F_P^{-1}}{D_c}\right)^{\lambda_5} \left(\dfrac{\kappa_s}{\kappa_h}\right)^{\lambda_6} N_T^{\lambda_7} & \text{if } N_T > 2 \text{ and } Re_{a,D_c} > 700. \end{cases} \tag{5.114}$$

where

$$\kappa_s = \begin{cases} 1.98 & \text{if slit-medium;} \\ 1.0 & \text{if superslit-low;} \\ 1.0 & \text{if superslit-high.} \end{cases} \tag{5.115}$$

$$\kappa_h = \begin{cases} 1.46 & \text{if slit-medium;} \\ 1.6 & \text{if superslit-low;} \\ 2.0 & \text{if superslit-high.} \end{cases} \tag{5.116}$$

$$\lambda_1 = -0.2555 - 0.0312 \left(\frac{D_c}{F_P^{-1}}\right) - 0.0487 N_T \tag{5.117}$$

$$\lambda_2 = 0.9703 - 0.0455\ \sqrt{Re_{a,D_c}} - 0.4986 \left[\log_e \left(\frac{S_T}{W_T}\right)\right]^2 \tag{5.118}$$

$$\lambda_3 = 0.2405 - 0.003 Re_{a,D_c} + 5.5349 \left(\frac{F_P^{-1}}{D_c}\right) \tag{5.119}$$

$$\lambda_4 = -0.535 + 0.017 \left(\frac{S_T}{W_T}\right) - 0.0107 N_T \tag{5.120}$$

$$\lambda_5 = 0.4115 + 5.5756 \sqrt{\frac{N_T}{Re_{a,D_c}}}\ \log_e \left(\frac{N_T}{Re_{a,D_c}}\right) + 24.2028 \sqrt{\frac{N_T}{Re_{a,D_c}}} \tag{5.121}$$

$$\lambda_6 = 0.2646 + 1.0491 \left(\frac{\kappa_s}{\kappa_h}\right) \log_e \left(\frac{\kappa_s}{\kappa_h}\right) - 0.216 \left(\frac{\kappa_s}{\kappa_h}\right)^3 \tag{5.122}$$

$$\lambda_7 = 0.3749 + 0.0046\ \sqrt{Re_{a,D_c}}\ \log_e\left(Re_{a,D_c}\right) - 0.0433\ \sqrt{Re_{a,D_c}} \qquad (5.123)$$

Lanced fins require the minimum free-flow frontal area calculated as in Eq.(5.19) [153].

5.2.1.6
Refrigerant-side single-phase pressure drop

To compute frictional pressure drop for single-phase flow in a tube, the Churchill correlation [160], with a Petukhov friction factor for smooth tubes [161], is considered. In enhanced internal surfaces, this form of friction factor expression is modified, with an increase of 25% in pressure loss being assumed for microfinned and cross-grooved tubes, as suggested by Brognaux et al. [147].

The Churchill correlation combines expressions for friction factor in both the laminar and turbulent flow regimes, whilst providing an estimate for the transition region [162]. Further, Churchill's model shows very good agreement with the Darcy-Weisbach [161] equation for laminar flow [162], whereas in the turbulent regime, a difference of around 0.5–2% is observed between the correlations by Churchill and Colebrook–White [163].

The pressure drop is calculated according to Eq.(5.124).

$$\Delta P_{rf,l} = \zeta_l \frac{l_l}{D_{rf}} \frac{G_{rf}^2}{2\rho_l} \qquad (5.124)$$

where l_l is the legth of the tube with liquid refrigerant, determined as follows:

$$l_l = f_l l \qquad (5.125)$$

Eq.(5.126) is used to compute the friction factor for the in-tube liquid flow.

$$\zeta_l = \begin{cases} \zeta_{l,sm} & \text{if smooth;} \\ \\ 1.25\ \zeta_{l,sm} & \text{if enhanced.} \end{cases} \qquad (5.126)$$

where

$$\zeta_{l,sm} = \begin{cases} \dfrac{64}{Re_{rf,l}} & \text{if } Re_{rf,l} < 2300; \\ \\ 8\left[\left(\dfrac{8}{Re_{rf,l}}\right)^{12} + \dfrac{1}{\left(\tau_{l,1} + \tau_{l,2}\right)^{1.5}}\right]^{1/12} & \text{if } Re_{rf,l} \geq 2300. \end{cases} \qquad (5.127)$$

and

$$\tau_{l,1} = \left\{ 2.457 \log \left[\frac{1}{\left(\frac{7}{Re_{rf,l}}\right)^{0.9} + 0.27\left(\frac{\epsilon}{D_{rf}}\right)} \right] \right\}^{16} \tag{5.128}$$

$$\tau_{l,2} = \left(\frac{37,530}{Re_{rf,l}}\right)^{16} \tag{5.129}$$

Regarding the pressure drop in the heat exchanger vapor zone, $\Delta P_{rf,v}$ is calculated in the same fashion of Eq. (5.124), considering, in this case, variables ζ_v, l_v, ρ_v, $\zeta_{v,sm}$, Re_v, $\tau_{v,1}$ and $\tau_{v,2}$, computed analogously as in Eqs. (5.126) to (5.129).

5.2.1.7
Refrigerant-side two-phase pressure drop

To compute pressure drop for condensation processes, a correlation by Choi et al. [164] is applied. The authors developed an expression, based on Pierre's pressure drop model [165], for evaporation and condensation in smooth and enhanced tubes, for both lubricant-free refrigerants and refrigerant/lubricant mixtures.

The two-phase pressure loss is represented as follows:

$$\Delta P_{rf,tp} = (\Delta P_{frc} + \Delta P_{acc}) \tag{5.130}$$

The friction contribution to the pressure loss is given by Eq. (5.131):

$$\Delta P_{frc} = \zeta_{tp} \frac{2G^*_{rf} l_{tp} v_{rf,avg}}{\xi_{dh}} \tag{5.131}$$

where G^*_{rf} is defined in Eq. (5.77), l_{tp} is the tube length with two-phase refrigerant, determined by Eq. (5.132), and $v_{rf,avg}$ is the refrigerant average specific volume in the tube, calculated by Eq. (5.133).

$$l_{tp} = f_{tp} l \tag{5.132}$$

$$v_{avg} = \frac{v_{in} + v_{out}}{2} \tag{5.133}$$

Further, the friction factor, ζ_{tp}, is calculated as in Eq. (5.134), whilst ξ_{dh}, a parameter dependent on the type of internal surface of the tube, can be obtained with Eq. (5.135).

$$\zeta_{tp} = 0.005058 \frac{\left(\frac{|h_{rf,v} - h_{rf,l}|\,|x_{rf,out} - x_{rf,in}|}{9.80665\ l_{tp}}\right)^{0.1554}}{\left(\frac{G^*_{rf}\xi_{dh}}{\mu_{rf,l}}\right)^{0.0951}} \tag{5.134}$$

$$\xi_{dh} = \begin{cases} D_{rf} & \text{if smooth;} \\ \\ \frac{4A_{sec}}{\xi_{sp}} & \text{if enhanced.} \end{cases} \tag{5.135}$$

where A_{sec} is defined in Eq. (5.72) and ξ_{sp} is determined as:

$$\xi_{sp} = \pi D_{rf} - \beta_4 \left[\xi_{ba} + \left({\xi_{ba}}^2 + 4{\beta_3}^2\right)^{0.5}\right] \tag{5.136}$$

$$\xi_{ba} = \frac{2\beta_3 \tan(0.5\beta_1)}{\cos\beta_2} \tag{5.137}$$

The acceleration contribution to the pressure loss is given by Eq. (5.138):

$$\Delta P_{acc} = |x_{rf,out} - x_{rf,in}| \frac{2G^*_{rf} v_{rf,avg}}{x_{qw}} \tag{5.138}$$

where x_{qw} is the average vapor quality.

5.2.1.8 Refrigerant charge

To calculate the total refrigerant mass in single and two-phase sections of a tube-and-fin heat exchanger, Eq.(5.139) is considered.

$$m_{rf} = m_{rf,l} + m_{rf,v} + m_{rf,tp} \tag{5.139}$$

where

$$m_{rf,l} = \left(\frac{\pi D_{rf}^2}{4} l_l N_{circ}\right)\left(\frac{1}{v_{rf,l}} + \frac{1}{v_{rf,out}}\frac{1}{2}\right) \tag{5.140}$$

and

$$m_{rf,v} = \left(\frac{\pi D_{rf}^2}{4} l_v N_{circ}\right)\left(\frac{1}{v_{rf,in}} + \frac{1}{v_{rf,v}}\frac{1}{2}\right) \tag{5.141}$$

For two-phase flow, Eq.(5.142) is considered, with the two-phase density being calculated in terms of the void fraction Φ.

$$m_{rf,tp} = \left(\frac{\pi D_{rf}^2}{4} l_{tp} N_{circ}\right)\left[\frac{1}{v_{rf,l}}(1-\Phi) + \frac{1}{v_{rf,v}}\Phi\right] \tag{5.142}$$

According to Assawamartbunlue and Brandemuehl [166], different models for void fraction calculation have been proposed by Rigot [167], Ahrens [168], Zivi [169], Smith [170], Lockhart and Martinelli [171], Baroczy [172], Tandom et al. [173], Hughmark [174], and Premoli et al. [175]. However, large variations in average two-phase density are verified when comparing the alternative models, with Rice [176] reporting that the average density can vary by a factor of 10 among them.

Notwithstanding, studies from Rice [176] and other researchers showed that the absolute accuracy of the void fraction model does not affect heavily performance prediction, mainly due to charge-sensitive systems “rebalancing” themselves at off-design conditions, besides the many interactions among system components [166]. Since different tube interbal surfaces are considered, correlations adapted to each condition are applied.

According to Honeywell [177], the correlations that provide smallest deviations in both condensation and evaporation processes for smooth tubes are those of Premoli et al. [175] and Smith [170]. Regarding two-phase flow in enhanced surfaces, Honeywell suggested [177] the application of Barozy’s [172], Hughmark’s [174] or Premoli et al.’s [175] correlations. In that sense, the four correlations mentioned are included for use in the model, with the potential user free to choose which expression to consider. When no specific choice is made regarding the void fraction calculation method, the model uses the Premoli et al. expression [175] for smooth tube, whilst, in enhanced tubes, Hughmark’s correlation [174] is applied, Eq.(5.143).

$$\Phi = \begin{cases} \Phi_{Prem} & \text{if smooth;} \\ \\ \Phi_{Hugh} & \text{if enhanced.} \end{cases} \tag{5.143}$$

Premoli et al. model According to Rice [176], the method developed by Premoli et al. [175] is mass flux-dependent and empirically based, and it was optimized to minimize liquid density prediction errors. The authors’ equations were given in terms of the slip ratio, ϕ_S, as described by Eq.(5.144).

$$\Phi_{Prem} = \frac{1}{1 + \dfrac{1 - x_{qw}}{x_{qw}} \dfrac{\rho_{rf,v}}{\rho_{rf,l}} \phi_S} \tag{5.144}$$

where

$$\phi_S = 1 + \phi_{F1} \left(\frac{\phi_y}{1 + \phi_{F2}\phi_y} - \phi_{F2}\phi_y \right)^{0.5} \tag{5.145}$$

$$\phi_{F1} = 1.578 \; Re_{rf,l}^{-0.19} \left(\frac{\rho_{rf,v}}{\rho_{rf,l}} \right)^{0.22} \tag{5.146}$$

$$\phi_{F2} = 0.0273 \; We_{rf,l} \; Re_{rf,l}^{-0.51} \left(\frac{\rho_{rf,v}}{\rho_{rf,l}} \right)^{-0.08} \tag{5.147}$$

$$\phi_y = \frac{\phi_{Be}}{1 - \phi_{Be}} \tag{5.148}$$

$$\phi_{Be} = \frac{1}{1 + \dfrac{1 - x_{qw}}{x_{qw}} \dfrac{\rho_{rf,v}}{\rho_{rf,l}}} \tag{5.149}$$

The refrigerant liquid Webber number $We_{rf,l}$ is defined as:

$$We_{rf,l} = \frac{G_{rf}^2 D_{rf}}{\sigma_{rf,l} \rho_{rf,l}} \tag{5.150}$$

Hugmark model The empirical Hughmark correlation [174] is a generalization of the work of Bankoff [178], assuming a bubble flow regime with a radial gradient of bubbles across the channel [176]. Results from Otaki [179] and Farzad and O'Neal [180] showed that the Hughmark method provides great comparison to experimental data [166]. The equations for the Hughmark model involve use of another form of the homogeneous equation,

$$\Phi_{Hugh} = \frac{\phi_i + \phi_{Cal}}{2} \tag{5.151}$$

$$\phi_{Cal} = \frac{\phi_{KH}}{1 + \dfrac{1 - x_{qw}}{x_{qw}} \dfrac{\rho_{r,v}}{\rho_{r,l}}} \tag{5.152}$$

where ϕ_{KH} is the added dependence, differentiating from the homogeneous equation where $\phi_{KH} = 1$. Eq.5.152 must be iteratively evaluated to obtain the void fraction at each refrigerant quality. Thus, because of the need for iteration, the Hughmark model is the most difficult method to use of those mentioned here. Its detailed escription can be found in Hughmark [174] and Rice [176].

5.2.2
Evaporator

In a similar fashion, a tube-and-fin evaporator from the same version of the ORNL Heat Pump Design Model [89] is considered for update.

The model approach for the evaporator is almost identical to that of the condenser, except for the air dehumidification algorithm and other inherent differences [89], which are further detailed in following sections. The assumption of equivalent parallel refrigerant circuits with unmixed flow on both the air and refrigerant sides is maintained, as well as the computation of parameters in distinct regions, now two: superheated and two-phase zones.

Figure 5.9 illustrates the two-zone approach for the evaporator modeling, whilst Figure 5.10 presents a block diagram with the organization and loops considered for model solution. The routines updated for the evaporator are similar to those of the condenser, and are listed in Section 5.2.1.

The updated mathematical model of the evaporator is described in the sections that follow.

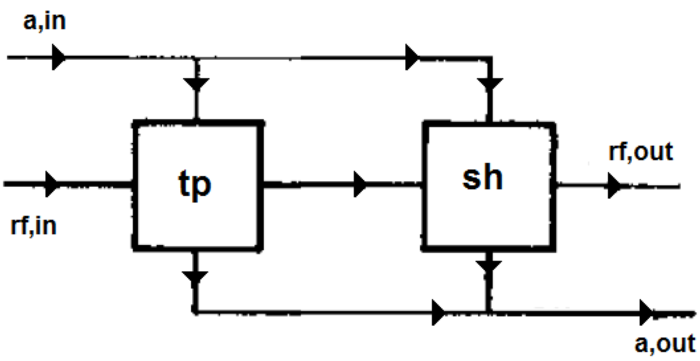

Figure 5.9: Schematic flow diagram for the multizone method applied to the evaporator, adapted from Martins Costa and Parise [95].

5.2.2.1 Heat exchanger geometric parameters

The geometry-related parameters associated to the evaporator model are analogous to those of the condenser, as an identical tube-and-fin heat exchanger is being considered. Thus, refer to Section 5.2.1.1 for details regarding the variables and algebra related to the geometry of the evaporator.

Figure 5.4 can also be used as reference for the physical structure of the evaporator.

5.2.2.2 Heat exchanger thermal performance

The performance of the evaporator is calculated with the computational sequence depicted in Figure 5.11.

Similarly to the condenser, heat transfer for the single-phase and two-phase refrigerant regions of the heat exchanger are calculated by means of effectiveness-NTU expressions. The number of transfer units and the effectiveness for the two-phase region of the evaporator are described by Eqs.(5.25) and (5.26), respectively.

It is assumed that, in case moisture removal is present (i.e., wet surface) in the heat exchanger, the phenomenon takes place on the two-phase portion of the coil only [89]. There is a check to verify, though, if the air exiting the superheated region of the heat exchanger is super-saturated [89], with a change in humidity ratio and associated parameters to appropriate values whenever this situation is confirmed to occur. The reader is advised to check the ORNL Heat Pump Design Model evaporator model [89] for more details regarding the heat transfer procedure in the situation of where dehumidification is present.

Moving on with the assumption of no moisture removal, calculation of the

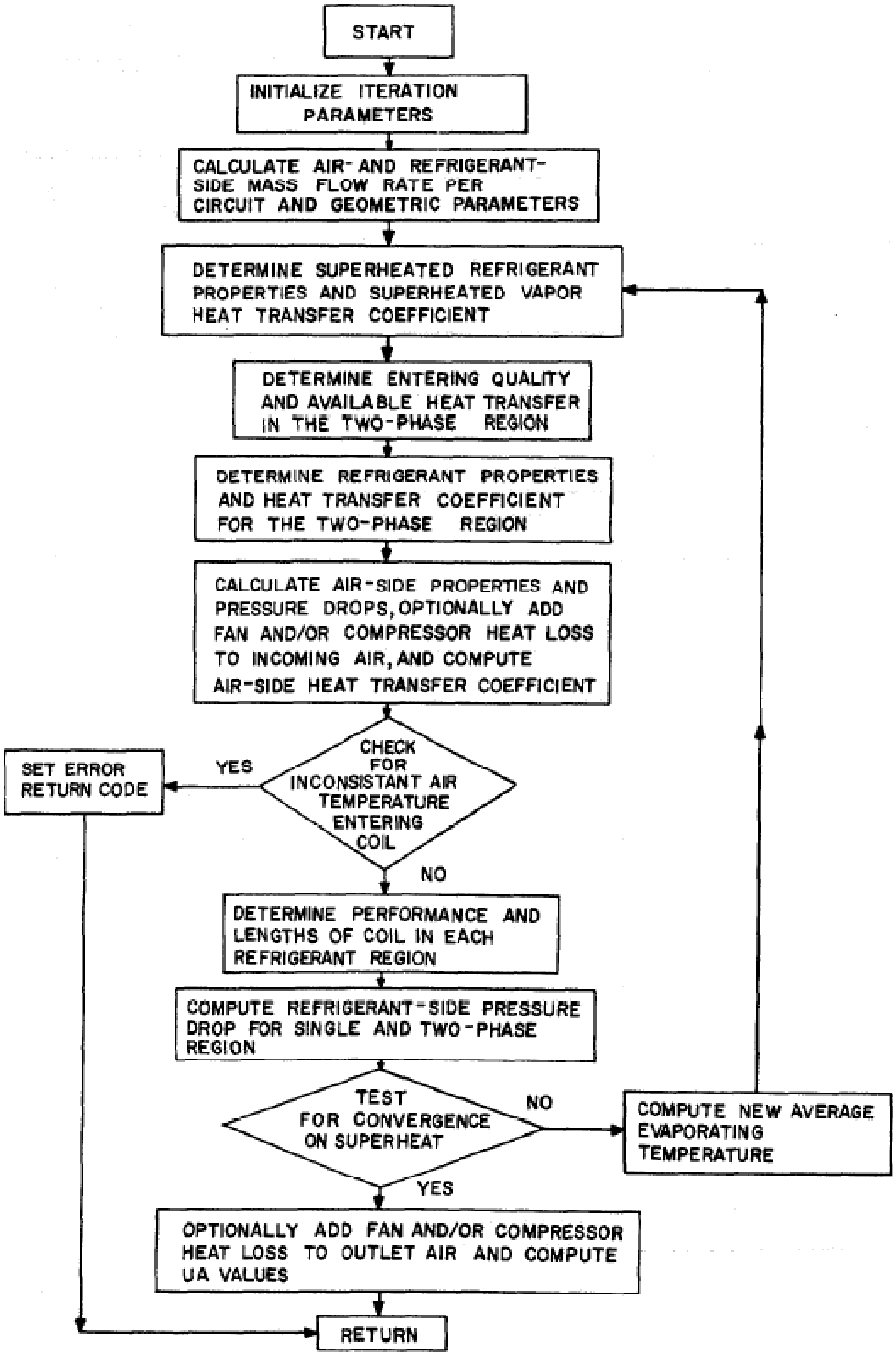

Figure 5.10: Structure and organization of the evaporator from the ORNL Heat Pump Design Model [89].

fraction of each coil with superheated and two-phase refrigerant is required for further heat transfer and pressure drop analysis. For the evaporator, Eq.(5.153)

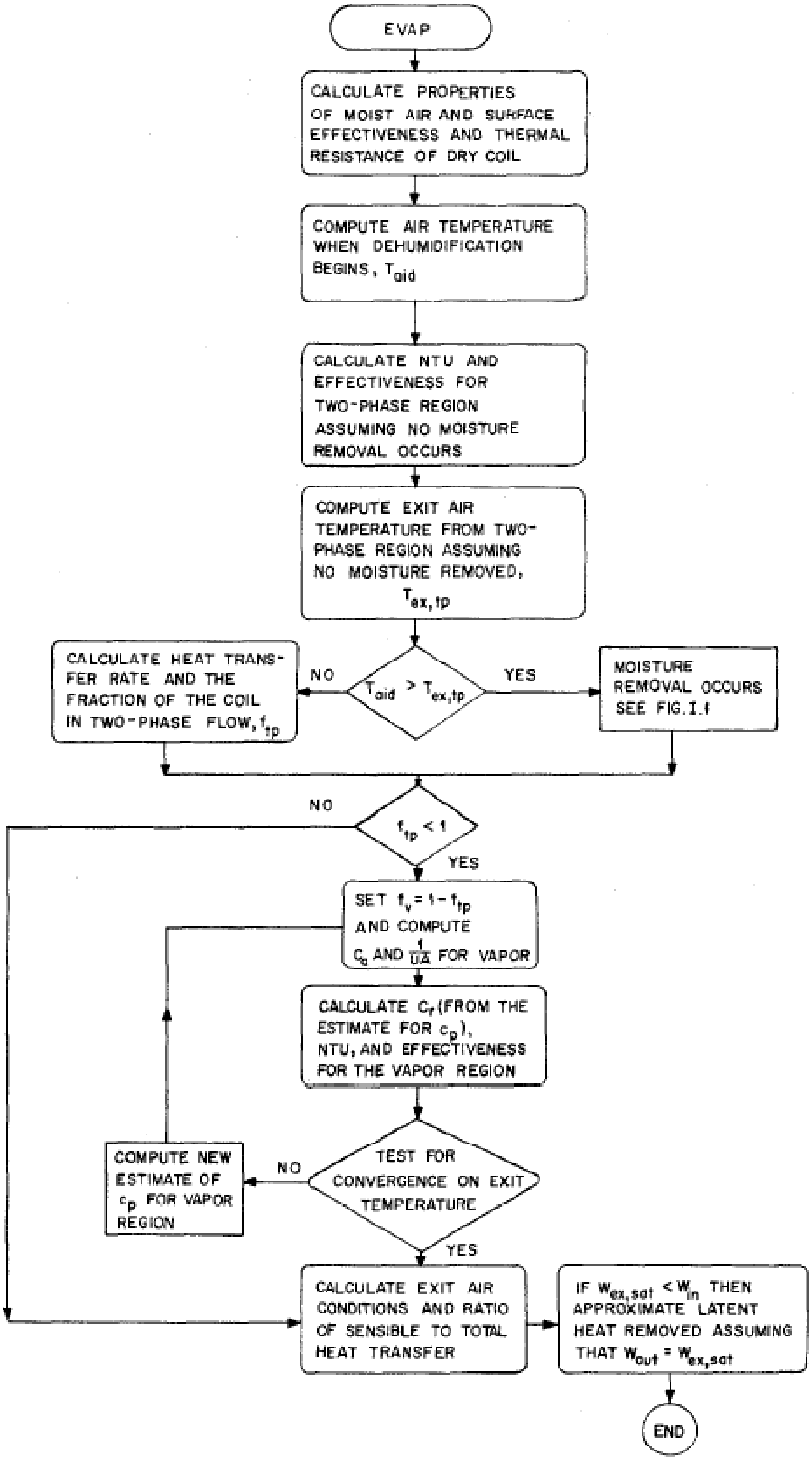

Figure 5.11: Block diagram for the evaporator performance calculation, adapted from the ORNL Heat Pump Design Model [89].

represents the heat transfer rate necessary to fully evaporate the refrigerant [89].

$$\dot{Q}_{tp} = m_{rf} h_{fg} \left(1 - x_{rf,in}\right), \tag{5.153}$$

where the enthalpy difference in the two-phase region, h_{fg}, is given by Eq.(5.30).

The mass flow rate of air required to achieve $\dot{Q}_{tp}$ and the fraction of the coil containing two-phase refrigerant, $\dot{m}_{a,tp}$ and f_{tp}, respectively, are expressed in Eqs.(5.33) and (5.34). If f_{tp} is greater than 1, one observes that the entire coil contains two-phase refrigerant.

According to Fischer and Rice [89], Eq.(5.36) provides the number of transfer units for the superheated portion of the heat exchanger, whereas the thermal resistance is determined from Eq.(5.38). Analogously to the condenser heat performance calculation, the effectiveness of the superheated region is obtained from Hiller and Glicksman's [85] approximate solution, which takes into consideration a cross-flow heat exchanger with both fluids unmixed, Eqs.(5.40) and (5.42).

Thus, the fraction of the evaporator in the vapor region is computed by Eq.(5.154). Nevertheless, the single-phase capacity rate depends on the refrigerant outlet temperature, an unknown variable. Therefore, an iteration process is required to determine the effectiveness and fraction of the coil in the superheated portion of the evaporator [89].

$$f_v = 1 - f_{tp} \tag{5.154}$$

To compute the heat exchange rate for the entire coil, the sum of rates for superheated and two-phase regions is determined. Eq.(5.153) describes the calculation of the two-phase heat transfer rate, while Eq.(5.48) presents that of the vapor region. Therefore,

$$\dot{Q} = \dot{Q}_{tp} + \dot{Q}_v \tag{5.155}$$

Then, from Fischer and Rice [89], Eqs.(5.52) and (5.54) are used to obtain the air-side temperature change for each section the heat exchanger. Evaporator outlet air temperature is computed by an energy balance equation, for a control volume encompassing the whole evaporator, Eq. (5.156)

$$T_{a,out} = T_{a,in} + \frac{\dot{Q}_{tp} + \dot{Q}_v}{\dot{m}_a c_{p,m}} \tag{5.156}$$

5.2.2.3
Refrigerant-side single-phase heat transfer coefficient

The refrigerant heat transfer coefficient in the superheated region of the evaporator is calculated with the same correlations used for the condenser, Section 5.2.1.3, except for when enhanced internal surfaces are present. The enhancement factor obtained by Huang [157], in the case of an evaporator, is calculated by Eq.(5.60).

$$E_h = 1.3833 - 2.500 \cdot 10^{-5} Re_{rf} + 1.6667 \cdot 10^{-9} Re_{rf}^2 \tag{5.157}$$

Thus, the combination of Eq.(5.57) with the enhancement factor calculated in Eq.(5.157) provides a model to determine the refrigerant single-phase heat transfer coefficient in the evaporator tubes.

5.2.2.4
Refrigerant-side two-phase heat transfer coefficient

The heat transfer coefficient for the evaporating refrigerant is determined based on Cavallini et al. [158], for showing good consistency with experimental data composed of evaporation for single fluids, azeotropic mixtures and zeotropic mixtures [159]. Eq.(5.16) describes the refrigerant two-phase heat transfer coefficient calculation for evaporator tubes.

$$\alpha_{tp} = 1.25 \cdot 10^{-3} \frac{\pi \alpha_{hv} + (6.283 - \pi) + \alpha_{hw}}{6.283} \tag{5.158}$$

where α_{hv} is the heat transfer coefficient for the vapor flow [156], and α_{hw} is the heat transfer coefficient in the wetted part of the tube, determined using Eqs.(5.159) and (5.160), respectively.

$$\alpha_{hv} = 0.023 Re_{rf,v}^{0.8} Pr_{rf,v}^{0.4} \frac{k_{rf,v}}{D_{rf}^*} \tag{5.159}$$

$$\alpha_{hw} = \alpha_{nb} + \alpha_{cb} \tag{5.160}$$

In the expression for the heat transfer coefficient on the wetted portion of the tube, parameters α_{nb} and α_{cb} refer, respectively, to the nucleate pool boiling component, Eq.(5.161), and the convective liquid flow boiling component, Eq.(5.165) of the process.

The nucleate pool boiling heat transfer is evaluated according to the Cooper correlation [181], considering the different types of internal tube surfaces, as outlined in the expressions below:

$$\alpha_{nb} = \begin{cases} \dfrac{55 P_{red}^{0.12} q^{0.67}}{\left(-\log_{10} P_{red}\right)^{0.55} M^{0.5}} & \text{if smooth;} \\ \\ s_{nb} \left(\dfrac{0.01}{D_{rf}^*}\right)^{0.38} \dfrac{55 P_{red}^{0.12} q^{0.67}}{\left(-\log_{10} P_{red}\right)^{0.55} M^{0.5}} & \text{if enhanced.} \end{cases} \tag{5.161}$$

where the reduced pressure, P_{red}, the heat flux, q, and the nucleate boiling supression factor, s_{nb}, are determined from Eqs.(5.162), (5.163), and (5.164), respectively.

$$P_{red} = \frac{P}{P_{crit}} \tag{5.162}$$

$$q = \dot{m}_{rf} h_{fg} \frac{|x_{rf,out} - x_{rf,in}|}{l \cdot \xi_{sp}} \tag{5.163}$$

$$s_{nb} = \frac{1.36}{0.36} \left(\frac{1 - x_{qw}}{x_{qw}}\right)^{0.9} \sqrt{\frac{\rho_{rf,v}}{\rho_{rf,l}}} \left(\frac{\mu_{rf,v}}{\mu_{rf,l}}\right)^{0.1} \tag{5.164}$$

Regarding the convective heat flow boiling contribution, the following set of equations is considered:

$$\alpha_{cb} = \begin{cases} 0.023\ Re_{rf,l}^{0.8}\ Pr_{rf,l}^{0.333}\ s_{cb}\ \dfrac{k_{rf,l}}{D_{rf}} & \text{if smooth;} \\ \\ 0.023\ Re_{rf,l}^{0.8}\ Pr_{rf,l}^{0.333}\ s_{cb}\ \dfrac{k_{rf,l}}{D_{rf}^*}\ Rx^{2.14} \left(Bo_{rf} \cdot Fr_{rf}\right)^{s_{ca}} \left(\dfrac{0.01}{D_{rf}^*}\right)^{0.59} \left(\dfrac{100}{G_{rf}^*}\right)^{0.36} & \text{if enhanced.} \end{cases} \tag{5.165}$$

where

$$s_{ca} = \begin{cases} -0.15 & \text{if } G_{rf}^* < 500; \\ \\ -0.21 & \text{if } G_{rf}^* \geq 500. \end{cases} \tag{5.166}$$

$$s_{cb} = \left[1 - x_{qw} + 2.63 x_{qw} \left(\frac{\rho_{rf,l}}{\rho_{rf,v}}\right)^{0.5}\right]^{0.8} \tag{5.167}$$

5.2.2.5
Air-side heat transfer coefficient

The heat transfer coefficient for the air-side of the evaporator dry region is calculated in similar fashion to that of the condenser. The assumption of different types of fins is also considered in the modeling of this parameter, with the studies of Wang et al. [150–153] serving as reference, once again.

Thus, correlations from Section 5.2.1.5 can be used to determine the air-side performance on the dry portion of flat, wavy, louvered and lanced fin-and-tube evaporators.

The air-side heat transfer coefficient for the wetted zone of the heat exchanger, $\alpha_{a,wet}$, due to dehumidification, is obtained according to Meyers [182], in terms of the dry coefficient, $\alpha_{a,dry}$, the air volume flow rate, $\dot{V}_a$, and the frontal area, A_c.

$$\alpha_{a,wet} = 1.067 \left(\frac{\dot{V}_a}{A_c} \right)^{0.101} \alpha_{a,dry} \tag{5.168}$$

It is assumed that this correlation also applies to wetted surfaces with wavy, louvered and lanced fins.

5.2.2.6 Refrigerant-side single-phase pressure drop

The model for determining the pressure drop in the refrigerant single-phase zone of the evaporator is similar to that of the condenser, described in Section 5.2.1.6. With that in mind, Eqs.(5.130) to (5.138) can be applied, considering the parameters associated to refrigerant flow in the evaporator.

5.2.2.7 Refrigerant-side two-phase pressure drop

Since the correlation developed by Choi et al. [164], and applied in Section 5.2.1.7, is valid for both evaporation and condensation processes, without loss of generality, Eqs.(5.130) to (5.138) can be used to determine the pressure loss during evaporation inside smooth or enhanced tubes.

5.2.2.8 Refrigerant charge

Determining refrigerant mass in single and two-phase sections of the tube-and-fin evaporator follows the same routine described for the condenser, Section 5.2.1.8. Correlations by Premoli et al. [175] and Hughmark [174] are considered, again, for smooth and enhanced tube internal surfaces, respectively.

5.2.3 Compressor

The sub-model for the compression device is based on the ANSI/AHRI Standard 540, which refers to the performance rating of positive displacement refrigerant compressors and compressor units [183]. In this model, which is straightforward and requires less development time, the performance curves of a given compressor are statistically adjusted with equations that comprise its mathematical model.

The model allows the user to define its own scroll, reciprocating or rotary compressor, characterized with the use of either compressor maps or performance data obtained from laboratory tests or commercial catalogs. The compressor input data comprise the geometry, capacity, power consumption and operating conditions observed during the calorimeter tests.

The main variables considered by the compressor model are refrigerating capacity, power consumption, mass flow rate and electrical current. These parameters are represented by a polynomial expression, Eq.(5.169), where Υ can represent mass flow rate, power input or current, and c_1 to c_{10} are adjustment coefficients for each of these four. Further, corrections for different degrees of superheat and extrapolation out of the fitting range are also included in the present model.

$$\begin{aligned} \Upsilon = c_1 + c_2\ T_{ev,dew} + c_3\ T_{cd,dew} + c_4\ T^2_{ev,dew} + \\ +\ c_5\ T_{ev,dew}\ T_{cd,dew} + c_6\ T^2_{cd,dew} + c_7\ T^3_{ev,dew} + \\ + c_8\ T_{cd,dew}\ T^2_{ev,dew} + c_9\ T_{ev,dew}\ T^2_{cd,dew} + c_{10}\ T^3_{cd,dew} \end{aligned} \tag{5.169}$$

The user has two options here:

(a) Enter the values for mass flow rate and power (or capacity and power) for each combination of condensing and evaporating temperatures (obtained from the performance table of a given compressor); or

(b) Input two sets of ten coefficients, each group referring to mass flow rate and power (or capacity and power).

Regardless of the selected alternative, the submodel will evaluate the isentropic and volumetric efficiencies associated to the compression device, in order to apply them to the operational conditions of the system.

For its simplicity, this model is applicable to compressors as part of a larger system, though limited, once defined the coefficients of the equations, exclusively to the tested compressor. Further, utilization of the model must be restricted to the operating conditions (ISO or AHRI) under which the experimental data were obtained, due to their empirical nature. Considering that its mathematical description is based on a polynomial equation, results with no practical meaning can be produced when the model is applied outside such conditions.

5.2.4
Expansion device

A simple model is applied for the expansion device, as for the refrigeration system considered, the thermal loads do not vary significantly. The expansion process is assumed adiabatic [129], and, since no work is done, from the energy conservation equation, the process is isenthalpic. Eq.(5.170) is, therefore, applied for the expansion device.

$$h_{in} = h_{out} \tag{5.170}$$

5.2.5
Lines

Models for the connecting lines are analytical, with both heat transfer and pressure drop processes evaluated using the average properties for the fluid. Input data correspond to geometric parameters (diameters and lengths of tubes and insulation) and characteristics of the materials (thermal conductivity and density). The models also predict two-phase flow inside the lines, for when there is incomplete condensation or evaporation in the heat exchangers.

Regarding heat transfer processes, refrigerant single-phase heat transfer coefficient in the pipe is determined from first principles [155] when fully developed laminar flow is verified, whilst for predicting the turbulent regime heat transfer coefficient, the Dittus-Boelter correlation [156] is considered. In the case of two-phase flow passing through the lines, correlation from Cavallini et al. [158] is applied for condensation, as explained in Section 5.2.1.4, whilst evaporation processes require use of another Cavallini et al. expression [158], which was further detailed in Section 5.2.2.4.

The air-side heat transfer coefficient is obtained from correlations for natural convection over horizontal or vertical cylinders [155], depending on the arrangement of the connecting lines.

For refrigerant pressure drop along the lines, both frictional and gravitational components are calculated. To compute the former, for in-tube single-phase flow, the Churchill correlation [160] coupled with Petukhov's friction factor [161], which was previously discussed in Section 5.2.1.6, is applied. When two-phase refrigerant is flowing through the pipe, the correlation by Choi et al. [164] is considered, as detailed in Section 5.2.1.7.

5.2.6 Refrigerant and air properties

For the refrigerant properties, the model uses look-up tables generated from REFPROP 9.0 [131], which display information from one table based on the value of a foreign-key field in another table. The reason for considering look-up tables in the lumped parameter model is to speed up the computational process. Calling REFPROP and obtaining properties, within the Fortran platform, takes computing time and slows down the program when there is a significant number of property calls, as in the lumped parameter model for the heat exchangers, specially when non-azeotropic refrigerant mixtures with large temperature glides are considered. In this sense, the application of look-up tables proved to be particularly efficient.

Further, to obtain air properties for the condenser lumped parameter model, expressions from ASHRAE 2009 Fundamentals Handbook [161] are used.

5.3 Input data

A detailed description of the input data necessary for simulating the direct expansion refrigeration system modeled above is presented. The set of data is organized by means of the component directly associated to, in order to identify the requirements of the model. In short, the physical characteristics of all devices (except the expansion valve), the ambient conditions (indoor and outdoor) and the operational data are provided as input data.

Adjustment factors were also considered for all the components, due to the necessity of calibrating the model once experimental data were available for validation.

Operational parameters. Parameters regarding the overall performance of the system are presented next.

1. Refrigerant
2. Outdoor ambient temperature ($T_{cd,a,in}$)
3. Indoor ambient temperature ($T_{ev,a,in}$)
4. Subcooling degree at condenser outlet
5. Superheating degree at evaporator outlet
6. Guess for condensation temperature

7. Guess for evaporating temperature
8. Number of similar compressors in parallel
9. Number of similar evaporators in parallel

Compressors. As discussed in Section 5.2.3, for compressor-related input data, the user has to provide the geometry, capacity, power consumption and operating conditions observed during the calorimeter tests, using either compressor maps or tabular performance data (c_1–c_{10}).

Heat exchangers. The set of data described next must be entered by the user for each of the two – condenser and evaporator – fin-and-tube heat exchangers.

1. Air volumetric flow rate ($\dot{V}_a$)
2. Relative humidity of the inlet air (w_{in})
3. Air heat transfer adjustment multiplier
4. Air pressure drop adjustment multiplier
5. Fan energy input rate
6. Refrigerant heat transfer adjustment multiplier
7. Refrigerant pressure drop adjustment multiplier
8. Tubes outer diameter (D_a)
9. Tubes inner diameter (D_{rf})
10. Thermal conductivity of the tubes
11. Thickness of the fins (δ)
12. Fin pitch in fins/m (F_P)
13. Thermal conductivity of the fins
14. Frontal area (A_c)
15. Number of tube rows in transverse direction (N_T)
16. Number of equivalent, parallel refrigerant circuits (N_{circ})
17. Contact conductance between fins and tubes

18. Transverse pitch (S_T)

19. Longitudinal pitch (W_T)

20. Number of return bends

21. Type of fins

    (a) flat; or

    (b) wavy with corrugation angle 9.76°; or

    (c) wavy with corrugation angle 10.76°; or

    (d) wavy with corrugation angle 11.76°; or

    (e) louvered with louver angle 13.50°; or

    (f) louvered with louver angle 24.47°; or

    (g) louvered with louver angle 24.89°; or

    (h) louvered with louver angle 25.00°; or

    (i) louvered with louver angle 28.15°; or

    (j) louvered with louver angle 30.24°; or

    (k) louvered with louver angle 39.45°; or

    (l) lanced and slit-medium; or

    (m) lanced and superslit-low; or

    (n) lanced and superslit-high.

22. Type of tube internal surface

    (a) smooth; or

    (b) micro-finned; or

    (c) cross-grooved.

    The parameters below are associated to enhanced surfaces, and must only be entered when the internal surface of the tubes is not smooth:

23. Fin angle (γ_1)

24. Helix angle (γ_2)

25. Height (γ_3)

26. Number of fins (γ_4)

Lines. The following set of parameters must be entered by the user for each of the three – discharge, liquid and suction – connecting lines.

1. Indicator for flow direction
   (a) straight; or
   (b) flowing down; or
   (c) flowing up.
2. Refrigerant-side height difference
3. Air dry bulb temperature
4. Air pressure
5. Indicator for type of ambient condition
   (a) relative humidity; or
   (b) absolute humidity; or
   (c) wet bulb temperature.

   The paremeter to be entered next is associated to the indicator selected immediately above, that is, a value must me entered for the exact parameter chosen to define ambient conditions:
6. Relative humidity or absolute humidity or wet bulb temperature
7. Refrigerant-side pressure drop calibration factor
8. Refrigerant-side heat transfer calibration factor
9. Tube lenght
10. Tube outside diameter
11. Thermal conductivity of tube material
12. Density of tube material
13. Tube thickness
14. Indicator for insulation
    (a) not insulated; or
    (b) insulated.

The parameters below are associated to insulated pipes and must only be entered when insulation is considered:

15. Thermal conductivity of insulation material
16. Density of insulation material
17. Insulation thickness

5.4 Numerical solution and computational code

Analogously to the strategy considered for the thermodynamic models, a computational code coupling the sub-models described was developed in Fortran language. As previously mentioned in Section 5.2.6, thermodynamic and transport properties of the fluids are calculated with look-up tables coupled REFPROP 9.0 [131].

Solution of the above system of equations is component-based, following the sequence pattern illustrated in Figures 5.12 and 5.13. It can be observed that two iterative processes take place during the solution of the system "outside" the submodels, with one of them nested inside the other. They are associated with the determination of the condensation and evaporation temperatures. The loop for obtaining the condensation temperature is repeated, until convergence, for each evaporating temperature assumed, as represented in Figure 5.12. A typical run of the program for a single design point simulation takes less than one minute in an Intel Pentium Dual CPU E2200 with 2.2GHz.

In the present model, the refrigerant operating conditions are internally determined by the thermodynamic interaction with indoor and outdoor ambient conditions. The simulation results provide the overall performance of the refrigeration cycle in terms of a number of efficiency-related parameters, as well as operational variables (cooling capacity, COP, EER, evaporation and condensation temperatures). In addition, detailed results for each of the components are presented, including local parameters and refrigerant states at inlet and outlet of each device.

5.5 Validation

Comparison with experimental data is based on empirical results provided by Sotomayor [184] and Honeywell [185]. Both tests were conducted in Honeywell's Buffalo Research Laboratory (Buffalo, NY, USA) for the direct expansion (DX) refrigeration system illustrated in Figure 5.14. The experimental setup is composed of two heat exchangers of the tube-and-fin type,

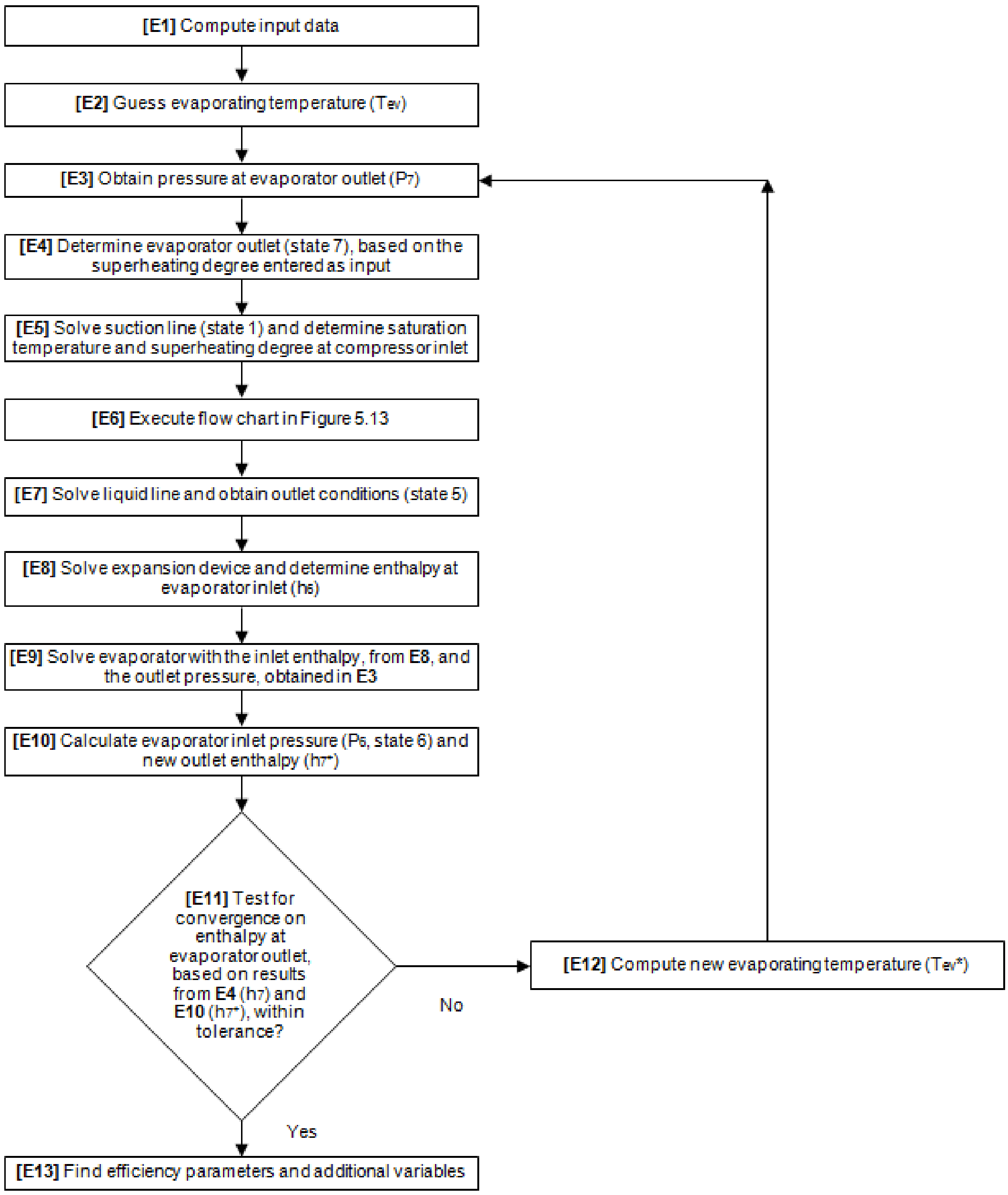

Figure 5.12: Computational sequence of the direct expansion model solution.

with smooth internal surfaces and wavy fins. A semi-hermetic compressor is also part of the apparatus, with a thermostatic valve working as the expansion device.

As it can be observed, the experimental facility presents additional devices that were not subject of analysis in the present theoretical model. Oil separator and receiver, flow meter, riser, accumulator and liquid receiver are part of the setup. Despite the operation of these devices reflecting on the behavior of the system, it is assumed, without loss of generality, that the results from this experimental apparatus are applicable for verification of the simulation model developed.

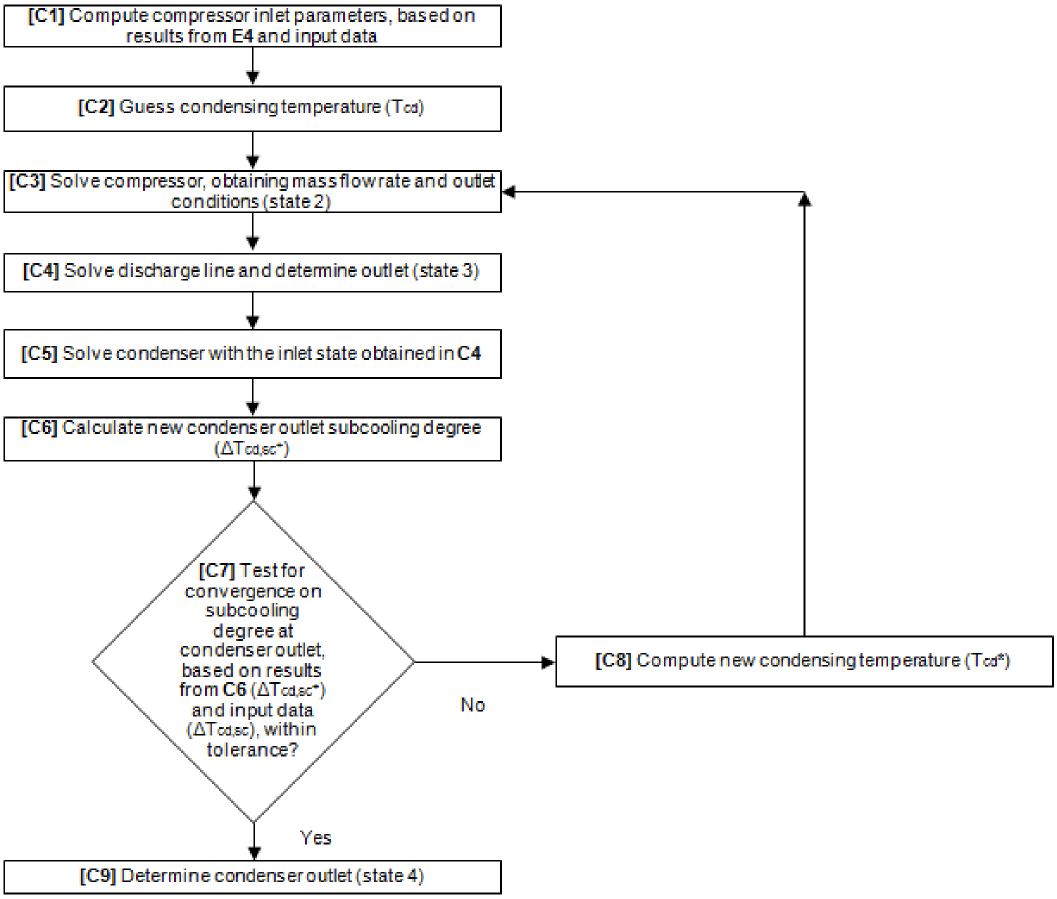

Figure 5.13: Computational sequence of the internal loop for determining condensing temperature.

The experimental data provided by Sotomayor [184] and Honeywell [185] comprises detailed information for refrigerant states at inlet and outlet of the components of the DX cycle operating with five different fluids: R22, R404A, R407F, HDR21 and HDR81. Four different tests were performed for each refrigerant, each one associated to a different indoor air ambient temperature, in order to provide results for distinct temperature levels. Another parameter that varies between the four tests is the superheating degree at evaporator outlet, with all other variables, from operational (outdoor ambient temperature and subcooling degree at condenser outlet, e.g.) to physical characteristics of the devices, remaining constant. For R404A, two additional tests with different values for outdoor ambient temperature were conducted in medium temperature level. In total, twenty-two design points were available.

Another important distinction between tests in medium and low temperature levels is the compressor selection. For medium temperature tests, Copeland refrigeration compressor KAKA-020A-TAC was considered, with power and volumetric displacement of 1491.4 W and 0.00201 m^3/s, respectively. In regard to the low temperature tests, Copeland's 2DF3-0300-TFC,

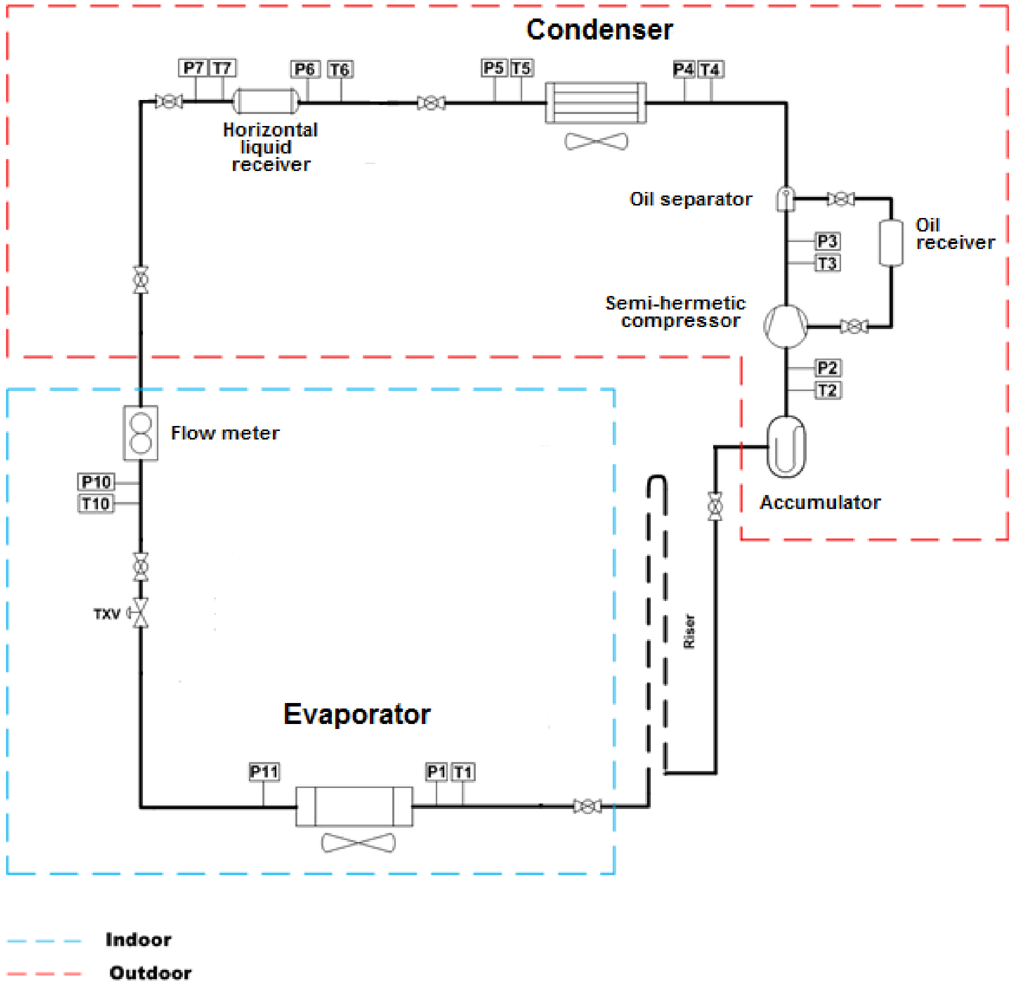

Figure 5.14: Schematic of the experimental setup for the direct expansion refrigeration system in Honeywell's Buffalo Research Laboratory, provided by Sotomayor [184].

with power of 2237.1 W and displacement of 0.00714 m^3/s, was selected. Performance data for the semi-hermetic compression devices was provided by Honeywell [185].

In that sense, two tables present the input data related to the experimental test. Table 5.1 shows the parameters which are constant for all the different design points, encompassing physical dimensions of the components, as well as operational variables, like subcooling degree at condenser outlet. Completing the set of input data, Table 5.2 depicts values for the parameters that vary between the twenty-two tests, including indoor air temperature, outdoor air temperature and evaporator superheating degree.

Comparison of results predicted by the model with experimental data is divided in two stages. First, a preliminary validation of the model is performed using the empirical results provided by Honeywell [185] for the DX cycle operating with R22. Figures 5.15 to 5.18 present the comparison between simulation and experimental results for the DX refrigeration system, operating with R22 in four different temperature levels. Theoretical and empirical data are compared, based on refrigerant states at inlet and outlet of the devices, as well as overall parameters like power input and mass flow rate, with precentual error and temperature difference as the main indicators.

Table 5.1: Part 1 of input data for direct expansion model verification – parameters that remain constant for all different design tests.

Parameter	**Value**
Condenser subcooling degree [°C]	0.00
Number of similar compressors in parallel	1
Number of similar evaporators in parallel	1
Condenser	
Air flow rate [m^3/s]	1.15
Relative humidity of inlet air [-]	0.4
Fan energy input rate [kW]	0.534
Outside diameter of the tubes [m]	0.009525
Inside diameter of the tubes [m]	0.008509
Thermal conductivity of the tubes [kW/m°C]	0.393
Thickness of the fins [m]	0.0001016
Fin pitch [fins/m]	393.701
Thermal conductivity of the fins [kW/m°C]	0.221
Frontal area [m]	0.6193536
Number of tube rows in transverse direction	3
Number of parallel refrigerant circuits	4
Contact conductance between fins and tubes [kW/m^2°C]	30.7
Transverse pitch [m]	0.0254
Longitudinal pitch [m]	0.022225
Number of return bends	68
Type of fins	wavy, angle 10.76°
Type of tube internal surface	smooth
Evaporator	
Air flow rate [m^3/s]	1.16
Relative humidity of inlet air [-]	0.4
Fan energy input rate [kW]	0.266
Outside diameter of the tubes [m]	0.0095504
Continued on next page	

Table 5.1 – continued from previous page

Parameter	Value
Inside diameter of the tubes [m]	0.0085344
Thermal conductivity of the tubes [kW/m°C]	0.393
Thickness of the fins [m]	0.0001016
Fin pitch [fins/m]	314.961
Thermal conductivity of the fins [kW/m°C]	0.221
Frontal area [m]	0.7838694
Number of tube rows in transverse direction	4
Number of parallel refrigerant circuits	7
Contact conductance between fins and tubes [kW/m^2°C]	30.7
Transverse pitch [m]	0.0254
Longitudinal pitch [m]	0.0254
Number of return bends	49
Type of fins	wavy, angle 10.76°
Type of tube internal surface	smooth
Discharge line	
Flow direction	straight
Refrigerant-side height difference [m]	0
Air temperature [°C]	35
Air pressure [kPa]	101.422
Air relative humidity [-]	0.4
Tube length [m]	13.5128
Tube outside diameter [m]	0.028575
Thermal conductivity of the tube material [kW/m°C]	0.393
Density of tube material [kg/m^3]	8910
Tube thickness [m]	0.001
Indicator for insulation	no insulation
Liquid line	
Flow direction	straight
Refrigerant-side height difference [m]	0
Air temperature [°C]	-26
Air pressure [kPa]	101.353
Air relative humidity [-]	0.4
Tube length [m]	11.4046
Tube outside diameter [m]	0.010791
Thermal conductivity of the tube material [kW/m°C]	0.393
Density of tube material [kg/m^3]	8910

Continued on next page

Table 5.1 – continued from previous page

Parameter	Value
Tube thickness [m]	0.001
Indicator for insulation	no insulation
Suction line	
Flow direction	straight
Refrigerant-side height difference [m]	0
Air temperature [°C]	35
Air pressure [kPa]	101.325
Air relative humidity [-]	0.4
Tube length [m]	2.4638
Tube outside diameter [m]	0.022225
Thermal conductivity of the tube material [kW/m°C]	0.393
Density of tube material [kg/m^3]	8910
Tube thickness [m]	0.001
Indicator for insulation	no insulation

With the results from the preliminary comparison, heat transfer and pressure drop adjustment factors were evaluated, in order to provide calibration for the simulation model, based on the experimental data for R22 in the DX cycle. Matching values were pursued for average condensing and evaporating temperatures, compressor suction pressure, power input and mass flow rate. Figure 5.19 shows the sequence considered for the process of calibrating the model. Different values for each multiplier were chosen for medium and low temperature applications, as exposed in Table 5.3, so as to take into consideration a possible tendency of the simulation model to produce better results for a specific temperature level.

The second stage of the validation process consists in comparing the results of the simulation model, now corrected with the adjustment factors, to the experimental data provided by Sotomayor [184] and Honeywell [185]. The empirical results used as reference are now associated with the DX refrigeration system operating with not only with R22 as test fluid, but also with R404A, R407F, HDR21 and HDR81. Figures 5.20 to 5.23 compare results obtained with experimental apparatus and simulation model, having considered in the latter, as mentioned, the adjustment multipliers previously estimated and exposed in Table 5.3. The comparison is performed in similar fashion to that of Figures 5.15 to 5.18.

Table 5.2: Part 2 of input data for direct expansion model verification – parameters that vary between the four different design tests.

Parameter (°C)	Test	R22	R404A	R407F	HDR21	HDR81
Outdoor ambient temperature	#1	35.0	35.0	35.0	35.0	35.0
	#2	35.0	35.0	35.0	35.0	35.0
	#3	35.0	35.0	35.0	35.0	35.0
	#4	35.0	35.0	35.0	35.0	35.0
	#5	—	26.7	—	—	—
	#6	—	26.7	—	—	—
Indoor ambient temperature	#1	10	10	10	10	10
	#2	1.7	1.7	1.7	1.7	1.7
	#3	−17.8	−17.8	−17.8	−17.8	−17.8
	#4	−26.1	−26.1	−26.1	−26.1	−26.1
	#5	—	10	—	—	—
	#6	—	1.7	—	—	—
Superheating degree	#1	5.56	6.00	4.15	3.92	3.56
	#2	5.33	5.39	3.89	3.70	3.56
	#3	5.40	6.02	5.41	6.00	4.94
	#4	2.57	2.38	4.03	4.73	2.83
	#5	—	6.06	—	—	—
	#6	—	6.09	—	—	—
Guess for condensing temp.	#1	41.8	41.1	42.8	40.1	42.6
	#2	40.0	39.1	41.0	40.6	40.8
	#3	42.1	41.1	42.2	41.6	42.3
	#4	40.1	39.2	40.4	39.7	40.5
	#5	—	34.7	—	—	—
	#6	—	32.8	—	—	—
Guess for evaporating temp.	#1	3.4	3.4	2.6	1.4	3.0
	#2	−4.5	−3.5	−5.4	−4.6	−4.7
	#3	−24.0	−23.4	−24.2	−24.2	−24.6
	#4	−30.4	−29.8	−31.8	−31.6	−31.1
	#5	—	−2.6	—	—	—
	#6	—	−4.3	—	—	—

As it can be observed in Figure 5.21(b), the percentual error between simulation results and experimental data for evaporator outlet pressure did not exceed 7.9%. Figures 5.22(b) and 5.23(a) show that relative discrepancy between experimental and predicted values for pressure at compressor discharge and expansion device inlet are, respectively, within the −6.6 to 0.2% and −5.7 to 0.8% ranges. Regarding refrigerant pressure at condenser inlet and outlet, discrepancies lie within ranges −6.1 to 0.8% and −6.1 to 3.4%, Figures 5.20(a) and 5.20(b), respectively.

When comparing the compressor suction pressure obtained with exper-

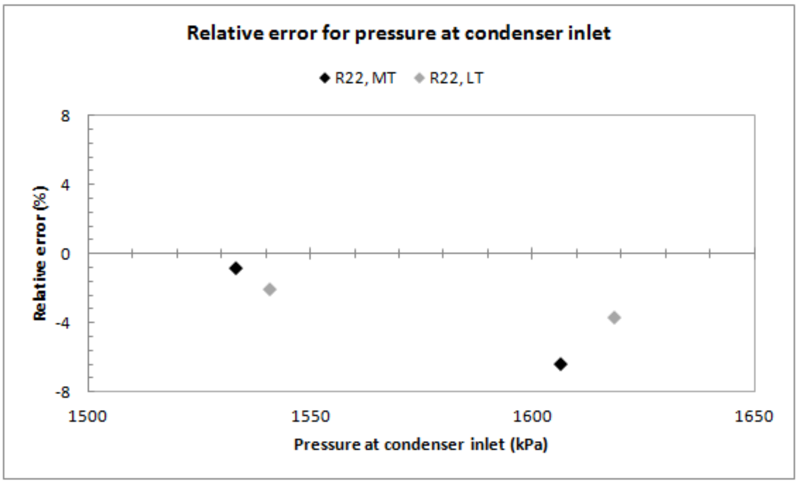

5.15(a): Condenser inlet pressure

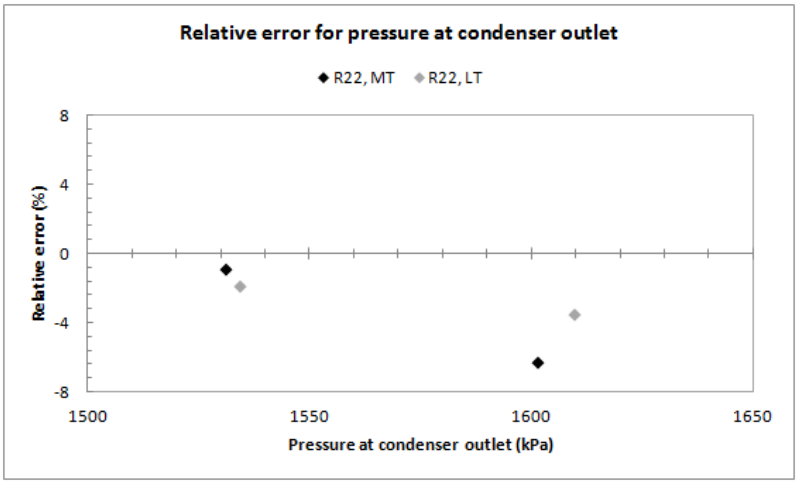

5.15(b): Condenser outlet pressure

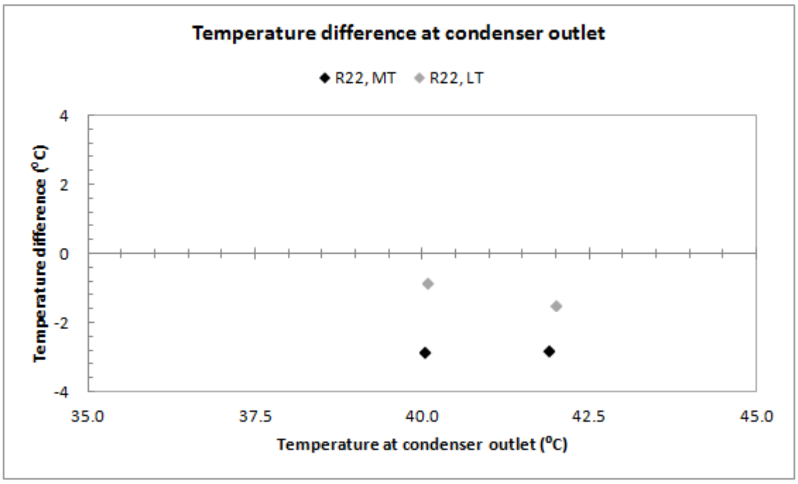

5.15(c): Condenser outlet temperature

Figure 5.15: Part 1 of comparison between direct expansion system simulation and experimental results, before applying the adjustment multipliers. Test data was provided by Honeywell [185] for DX refrigeration system operating with R22 in both medium and low temperature levels.

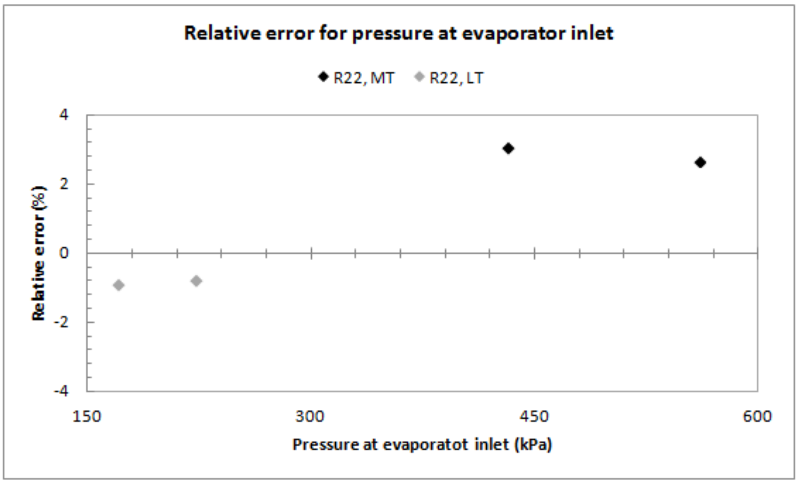

5.16(a): Evaporator inlet pressure

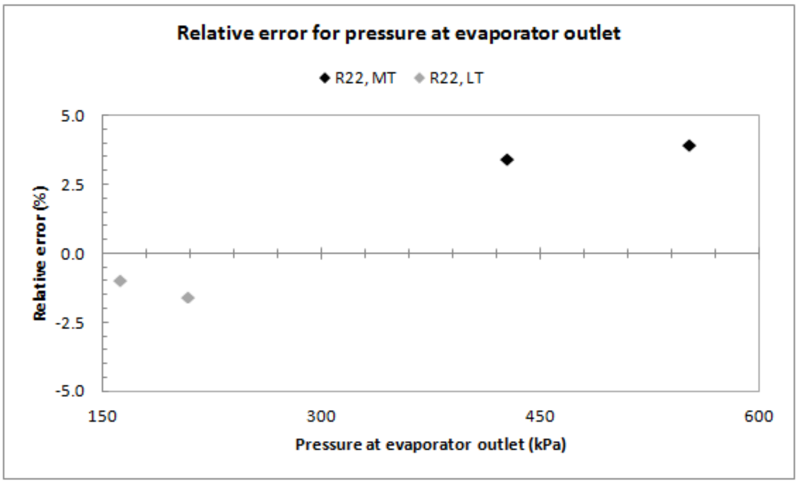

5.16(b): Evaporator outlet pressure

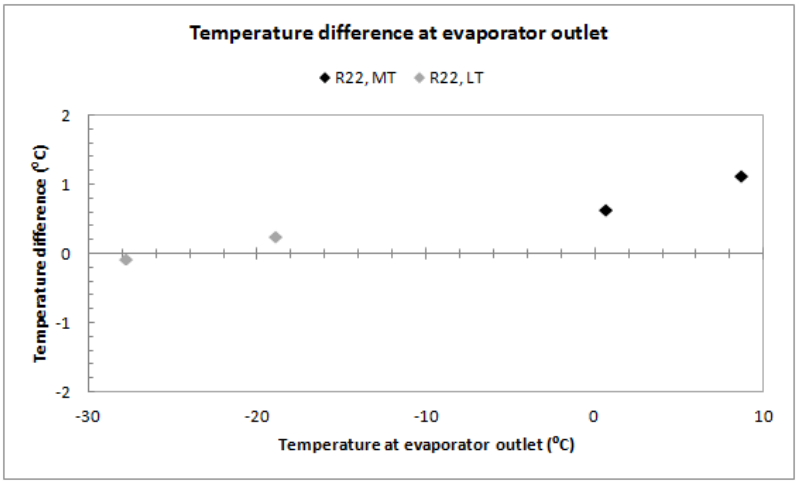

5.16(c): Evaporator outlet temperature

Figure 5.16: Part 2 of comparison between direct expansion system simulation and experimental results, before applying the adjustment multipliers. Test data was provided by Honeywell [185].

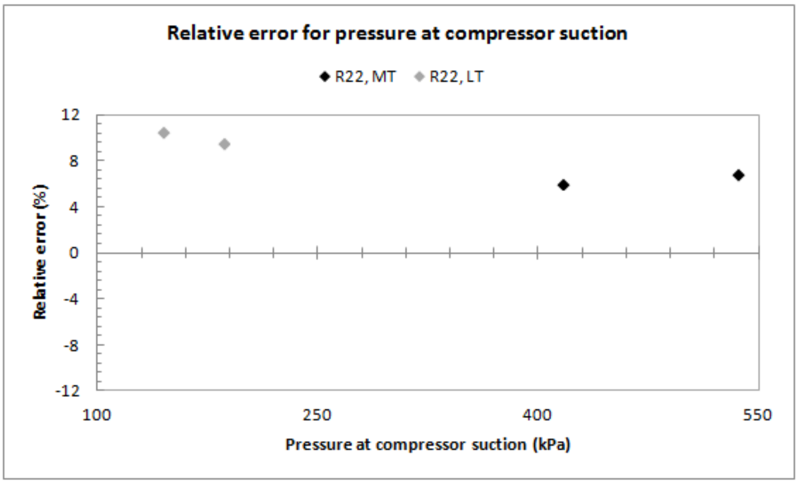

5.17(a): Compressor suction pressure

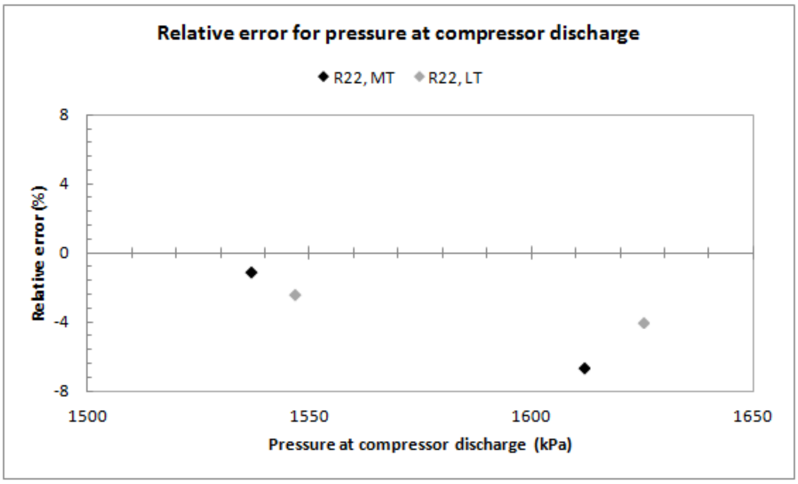

5.17(b): Compressor discharge pressure

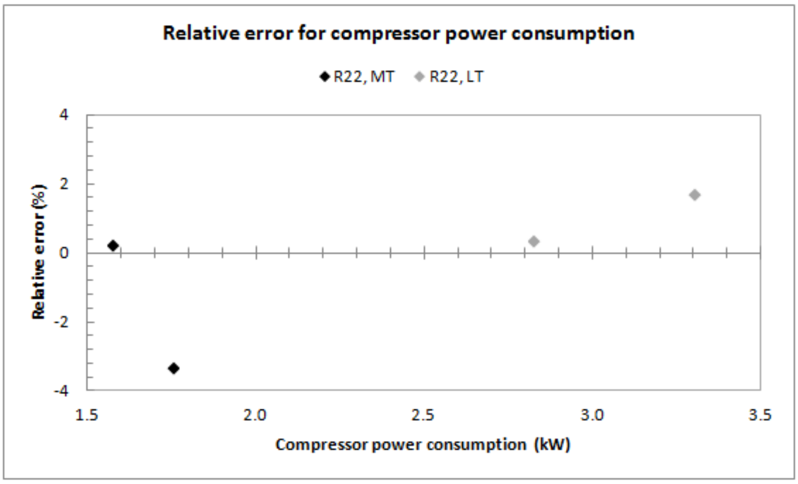

5.17(c): Compressor power consumption

Figure 5.17: Part 3 of comparison between direct expansion system simulation and experimental results, before applying the adjustment multipliers. Test data was provided by Honeywell [185].

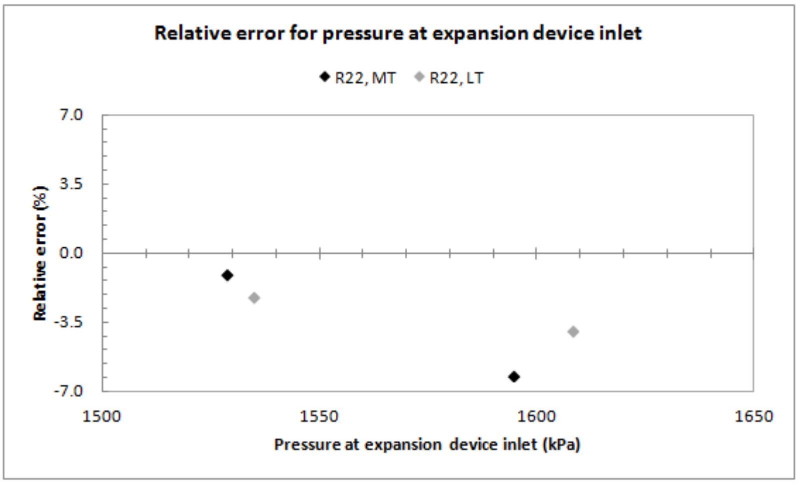

5.18(a): Expansion device inlet pressure

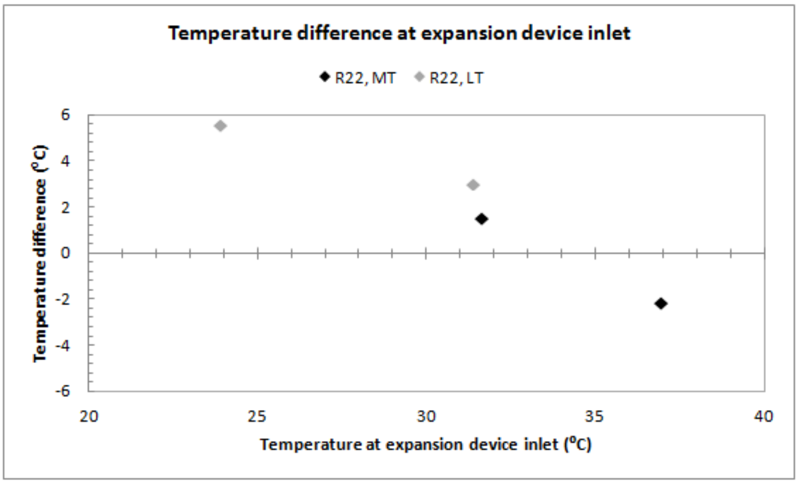

5.18(b): Expansion device outlet temperature

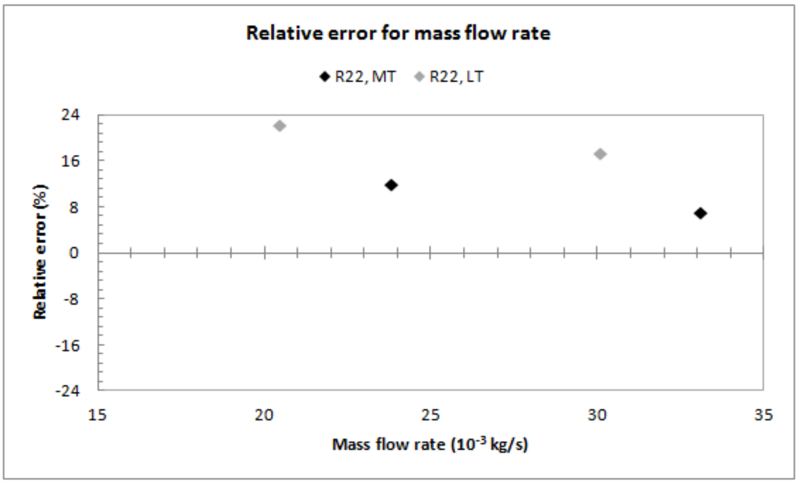

5.18(c): Mass flow rate

Figure 5.18: Part 4 of comparison between direct expansion system simulation and experimental results, before applying the adjustment multipliers. Test data was provided by Honeywell [185].

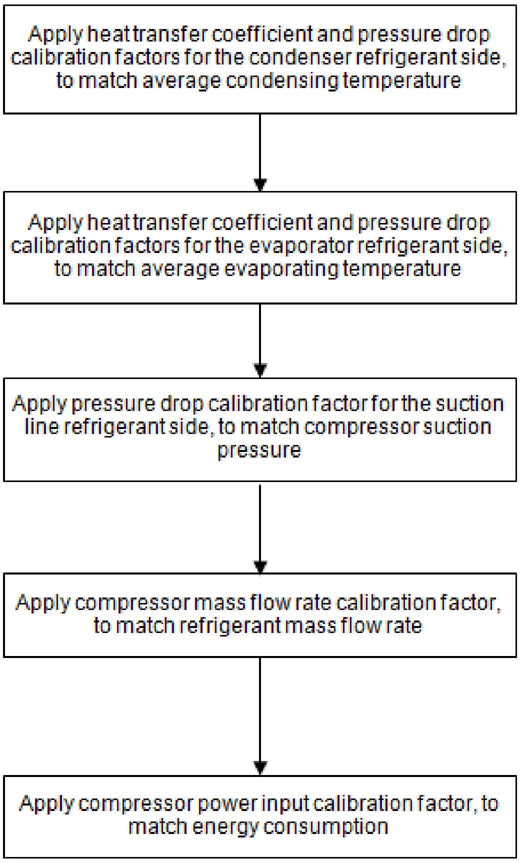

Figure 5.19: Sequence of steps followed to determine adjustment multipliers for the direct expansion cycle, based on experimental data.

Table 5.3: Values for simulation model adjustment multipliers in medium and low temperature applications.

Calibration factor	MT	LT
Condenser heat transfer	0.75	0.75
Condenser pressure drop	1.13	1.23
Evaporator heat transfer	1.25	1.25
Evaporator pressure drop	0.75	0.75
Suction line pressure drop	1.25	1.25
Compressor mass flow rate	0.76	0.80
Compressor power input	1.23	1.20

imental and simulation models, relative errors between 11.2 and 15.4% were verified for low temperature applications, whilst in medium temperature levels the discrepancy did not exceed 7.9%, Figure 5.22(a). A similar trend is observed for the pressure at evaporator inlet, Figure 5.21(a): in low temperatures, percentual errors lie between −14.4 and 0.3%, whereas lower and upper bounds are, respectively, −0.1 and 3.0% for medium temperature levels. Such results indicate that, for most refrigerants, the model predicts worse results for low temperature applications. A number of factors may influence this large discrepancy. They include the range of application of heat transfer and pressure drop correlations, which better represent physical process, apparently, in medium temperature levels.

For comparison of refrigerant temperature at evaporator outlet, experimental and theoretical values differ of less than 1.8°C, with only one test point for R404A in low temperature presenting 3.1°C of temperature difference, Figure 5.21(c). When the condenser exit temperature is considered, relative discrepancies between predicted and experimental results are more widely distributed, ranging from 0.0 to 2.6°C, Figure 5.20(c). Lower and upper bounds of the temperature discrepancy between experimental and theoretical models were of −2.0 and 2.2°C, respectively, at the expansion device inlet in medium temperature. In low temperature levels, differences can go up to 5.3°C, which reafirms the model ability to produce better predictions for medium temperature applications.

Analysing the results for compressor energy consumption, the percentual discrepancy between simulation results and experimental data varies between −3.1 to 5.7%. Errors of great magnitude were found in the refrigerant mass flow rate predictions, with discrepancy within the −17.3 and 17.4% range. It should be noted, as previously mentioned, that a few existing components in the experimental setup were not taken into account in the modeling effort, which may have affected the mass flow rate predictions. Further, compressor and expansion device modeling may require some improvement, as both components affect significantly the value of refrigerant mass flow rate. Suction pressure also presented prediction errors of a somewhat large magnitude, although it is not clear if it would be a cause or consequence in the refrigerant mass flow rate prediction.

Finally, it should be stressed that, for LCCP calculation purposes, which is the main goal of this study, the most relevant parameter is the compression power consumption, whose discrepancy magnitude did not exceed 6%. One can conclude that the model, in its present form, is an useful tool for the prediction of environmental impact of commercial DX refrigeration systems.

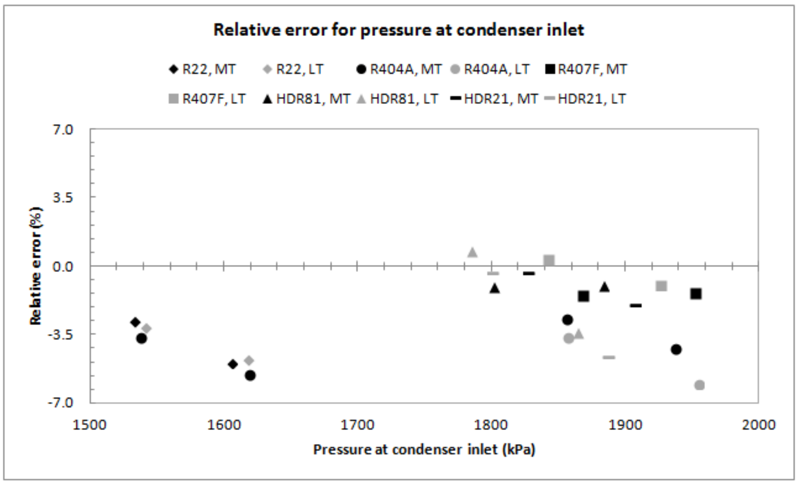

5.20(a): Condenser inlet pressure

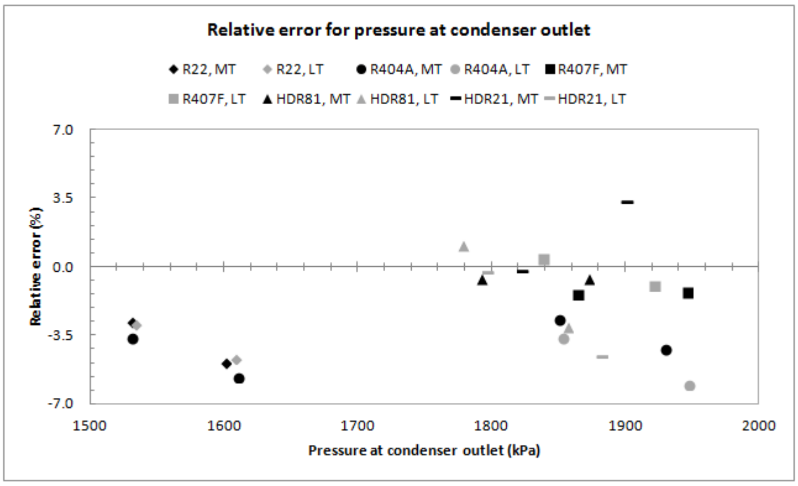

5.20(b): Condenser outlet pressure

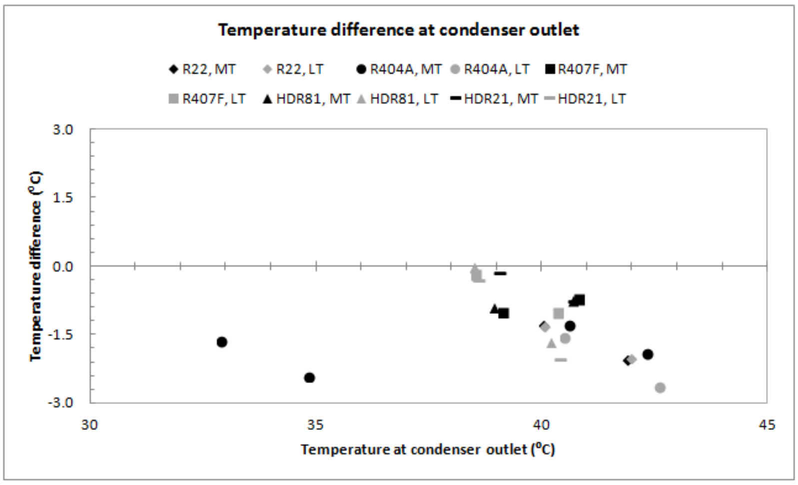

5.20(c): Refrigerant temperature at condenser outlet

Figure 5.20: Part 1 of comparison between direct expansion system simulation and experimental results, after applying the adjustment multipliers. Test data was provided by Sotomayor [184] and Honeywell [185] for DX refrigeration system operating with R22, R404A, R407F, HDR21 and HDR81 in both medium and low temperature levels.

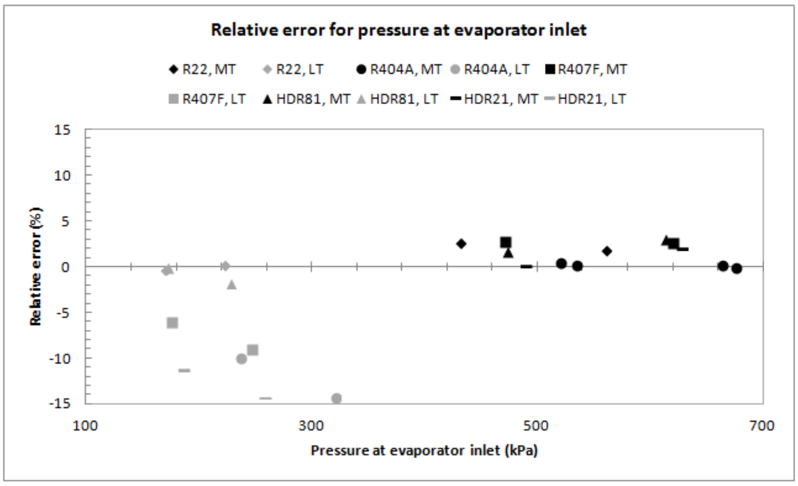

5.21(a): Evaporator inlet pressure

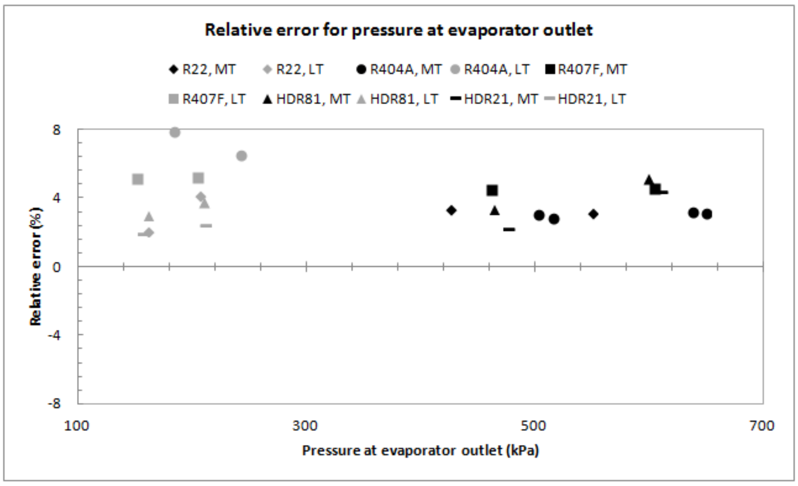

5.21(b): Evaporator outlet pressure

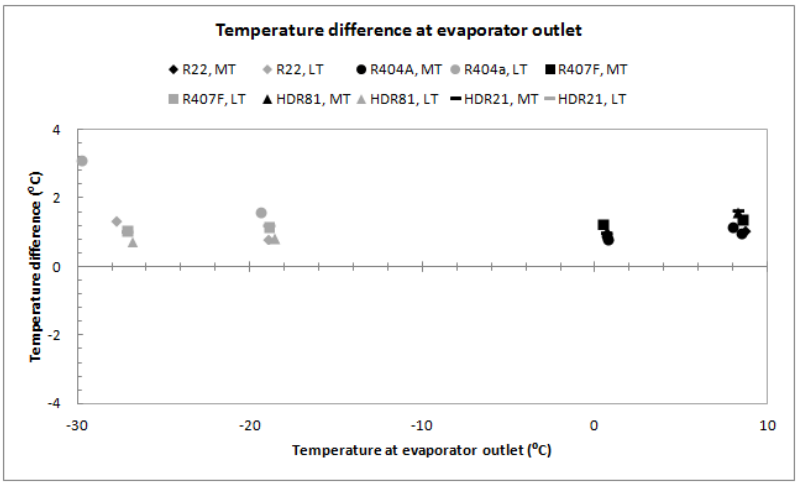

5.21(c): Refrigerant temperature at evaporator outlet

Figure 5.21: Part 2 of comparison between direct expansion system simulation and experimental results, after applying the adjustment multipliers. Test data was provided by Sotomayor [184] and Honeywell [185].

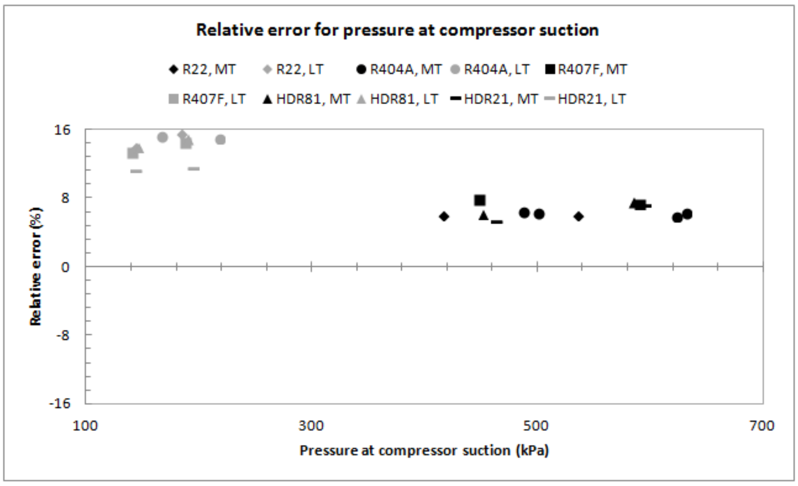

5.22(a): Compressor suction pressure

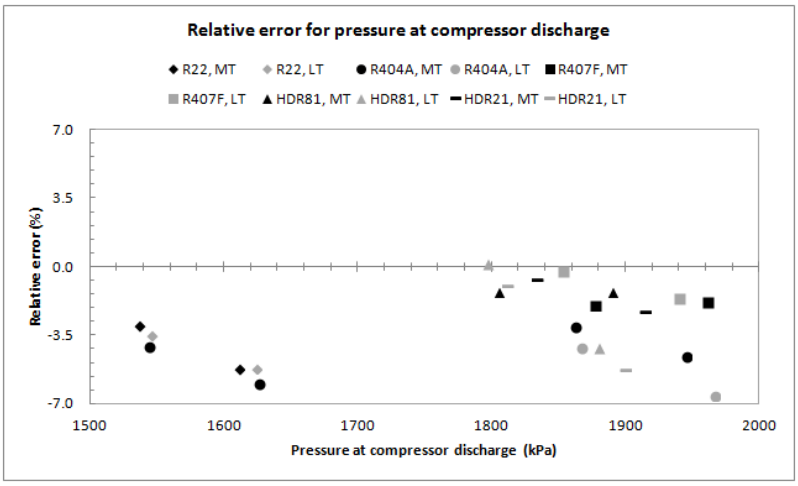

5.22(b): Compressor discharge pressure

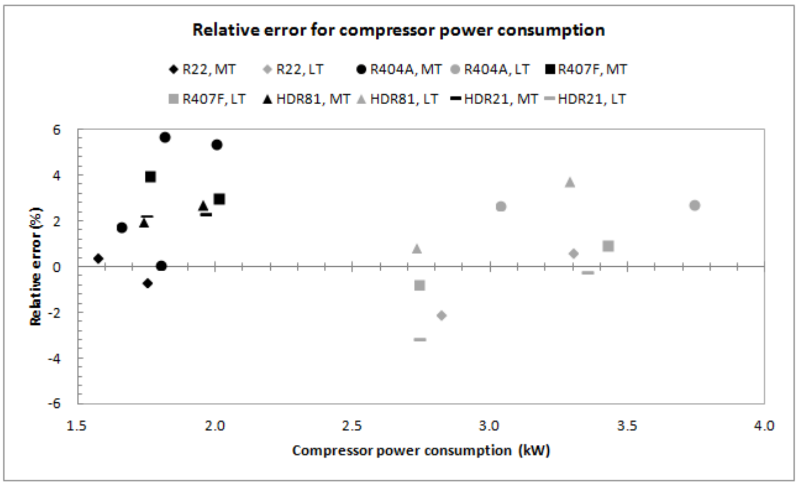

5.22(c): Compressor power consumption

Figure 5.22: Part 3 of comparison between direct expansion system simulation and experimental results, after applying the adjustment multipliers. Test data was provided by Sotomayor [184] and Honeywell [185].

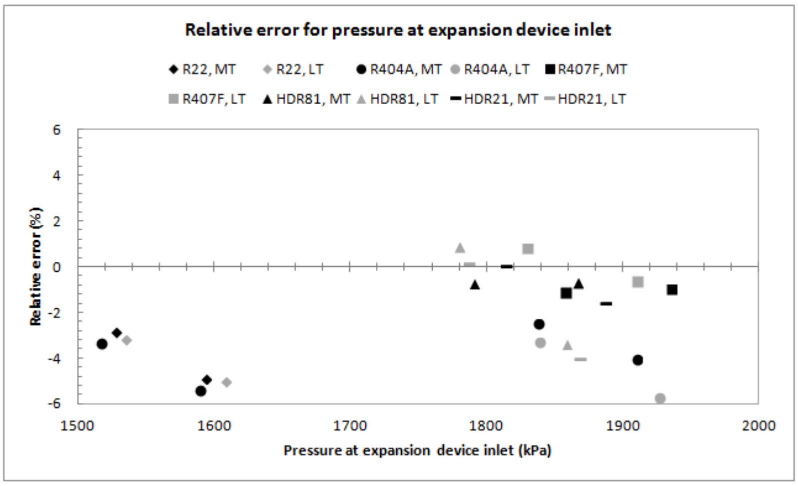

5.23(a): Expansion device inlet pressure

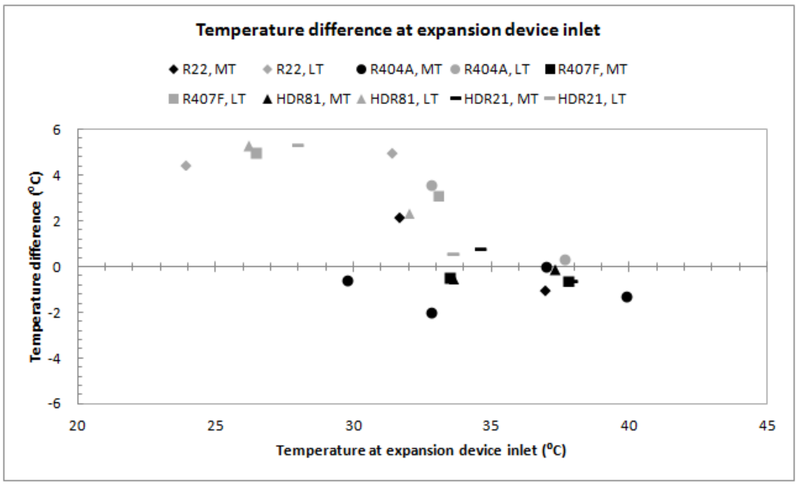

5.23(b): Refrigerant temperature at expansion device outlet

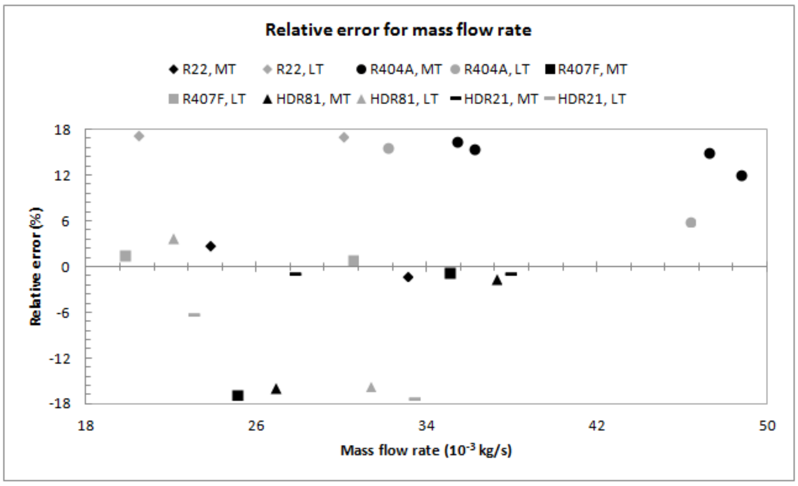

5.23(c): Mass flow rate

Figure 5.23: Part 4 of comparison between direct expansion system simulation and experimental results, after applying the adjustment multipliers. Test data was provided by Sotomayor [184] and Honeywell [185].